Evaluating Model Parameterizations of Submicron Aerosol Scattering and Absorption with In Situ Data from ARCTAS 2008

M. J. Alvarado[1], C. R. Lonsdale[1], H. L. Macintyre[2,*], H. Bian[3,4], M. Chin[4], D. A. Ridley[5], C. L. Heald[5,6], K. L. Thornhill[7], B. E. Anderson[7], M. J. Cubison[8,], J. L. Jimenez[8], Y. Kondo[9], L. K. Sahu[9], J. E. Dibb[10], and C. Wang[2]**

[1]{Atmospheric and Environmental Research, Lexington, Massachusetts, USA}

[2]{Center for Global Change Science, Massachusetts Institute of Technology, Cambridge, Massachusetts, USA}

[3]{Goddard Earth Sciences and Technology Joint Center for Earth Systems Technology, University of Maryland Baltimore County, Baltimore, Maryland, USA}

[4]{NASA Goddard Space Flight Center, Greenbelt, Maryland, USA}

[5]{Department of Civil and Environmental Engineering, Massachusetts Institute of Technology, Cambridge, Massachusetts, USA}

[6]{Department of Earth, Atmospheric and Planetary Science, Massachusetts Institute of Technology, Cambridge, Massachusetts, USA}

[7]{NASA Langley Research Center, Hampton, Virginia, USA}

[8]{Department of Chemistry and Biochemistry, and Cooperative Institute for Research in the Environmental Sciences, University of Colorado, Boulder, Colorado, USA}

[9]{Department of Earth and Planetary Science, University of Tokyo, Tokyo, Japan}

[10]{Department of Earth Sciences and Institute for the Study of Earth, Oceans, and Space, University of New Hampshire, Durham, New Hampshire, USA}

[*]{Now at Public Health England, Chilton, Oxfordshire, UK}

[**]{Now at Tofwerk AG, Thun, Switzerland}

Correspondence to: M. J. Alvarado (malvarad@aer.com)

1 **Abstract**

2 Accurate modeling of the scattering and absorption of ultraviolet and visible radiation by

3 aerosols is essential for accurate simulations of atmospheric chemistry and climate. Closure

4 studies using in situ measurements of aerosol scattering and absorption can be used to

5 evaluate and improve models of aerosol optical properties without interference from model

6 errors in aerosol emissions, transport, chemistry, or deposition rates. Here we evaluate the

7 ability of four externally mixed, fixed size distribution parameterizations used in global

8 models to simulate submicron aerosol scattering and absorption at three wavelengths using in

9 situ data gathered during the 2008 Arctic Research of the Composition of the Troposphere

10 from Aircraft and Satellites (ARCTAS) campaign. The four models are the NASA Global

11 Modeling Initiative (GMI) Combo model, GEOS-Chem v9-02, the baseline configuration of a

12 version of GEOS-Chem with online radiative transfer calculations (called GC-RT), and the

13 Optical Properties of Aerosol and Clouds (OPAC v3.1) package. We also use the ARCTAS

14 data to perform the first evaluation of the ability of the Aerosol Simulation Program (ASP

15 v2.1) to simulate submicron aerosol scattering and absorption when in situ data on the aerosol

16 size distribution is used, and examine the impact of different mixing rules for black carbon

17 (BC) on the results. We find that the GMI model tends to overestimate submicron scattering

18 and absorption at shorter wavelengths by 10-23%, and that GMI has smaller absolute mean

19 biases for submicron absorption than OPAC v3.1, GEOS-Chem v9-02, or GC-RT. However,

20 the changes to the density and refractive index of BC in GC-RT improve the simulation of

21 submicron aerosol absorption at all wavelengths relative to GEOS-Chem v9-02. Adding a

22 variable size distribution, as in ASP v2.1, improves model performance for scattering but not

23 for absorption, likely due to the assumption in ASP v2.1 that BC is present at a constant mass

24 fraction throughout the aerosol size distribution. Using a core-shell mixing rule in ASP

25 overestimates aerosol absorption, especially for the fresh biomass burning aerosol measured

26 in ARCTAS-B, suggesting the need for modeling the time-varying mixing states of aerosols

27 in future versions of ASP.

28

1 Introduction

Atmospheric aerosols can both scatter and absorb ultraviolet and visible (UV-VIS) light, thereby altering the actinic flux and the rates of photolytic reactions in the atmosphere (e.g., Michelangeli et al., 1992; He and Carmichael, 1999). The absorption of UV-VIS light by atmospheric aerosols is dominated by light absorbing carbon (LAC) and mineral dust particles (Bian et al., 2003; Martin et al., 2003). Produced by the incomplete combustion of fossil fuels and biomass, LAC has two major forms: "black carbon" or BC, which is primarily composed of soot; and organic aerosols (OA) that strongly absorb UV-VIS light, called "brown carbon" or BrC (Andreae and Gelencsér, 2006). Both forms of LAC can be internally mixed with or coated by less absorbing, more reflective inorganic and organic species, altering their optical properties (e.g., Liao et al., 1999; Yang and Levy, 2004; Lack and Cappa, 2010).

In situ and regional studies of the impact of LAC aerosols on photolysis rates have found that absorbing aerosols can reduce local photolysis rates and OH concentrations by as much as 40% (Tang et al., 2003; Lefer et al., 2003; Alvarado et al., 2009), substantially reducing the net production rate of O_3 in urban airsheds (Jacobson, 1998; Li et al., 2005) and biomass burning plumes (Tang et al., 2003; Alvarado et al., 2009), with the magnitude of the impact dependent on the concentrations of NO_x and VOCs (He and Charmichael, 1999; Yang and Levy, 2004). Global modeling studies have found similar impacts of LAC on photolysis rates, OH concentrations, and net O_3 production (e.g., Liao et al., 2003). For example, Bian et al. (2003) found that the scattering and absorption of UV-VIS light by aerosols increased global tropospheric mean O_3 by ~1 ppbv and decreased OH by 8%. Martin et al. (2003) found that the light absorption by externally mixed black carbon aerosols decreased the modeled photolysis rate of O_3 to form $O(^1D)$ by a factor of 2 in biomass burning regions and the Ganges Valley, thus decreasing OH concentrations by as much as 40%. Tie et al. (2005) found 10 to 40% reductions in the formation of $O(^1D)$ by photolysis in Europe, eastern Asia, and the Amazon due to externally mixed anthropogenic and biomass burning aerosols. This caused 5 to 40% reductions in HO_x concentrations along with modest changes to O_3 (-4 to +5%).

Furthermore, the scattering and absorption of UV-VIS light by LAC aerosols can lead to a significant climate forcing (the direct effect), but the magnitude of this forcing is uncertain. For example, the review of Bond et al. (2013) estimated the direct radiative forcing (DRF) of atmospheric BC is +0.71 W m^{-2} with 90% uncertainty bounds of (+0.08, +1.27) W m^{-2}.

3

1   Chung et al. (2012) used data from the ground based Aerosol Robotic Network (AERONET,

2   Dubovik and King, 2000) to estimate a similar global DRF of 0.65 ± 0.15 W m^{-2} from all

3   LAC aerosols, but in this study brown carbon was estimated to account for ~20% of the total

4   forcing. However, Wang et al. (2014) used the GC-RT model (Heald et al., 2014) combined

5   with AERONET data to obtain a lower DRF estimate of 0.32 W m^{-2} from all LAC aerosols

6   (uncertainty range 0.04 to 0.50 W m^{-2}), with 34% of the forcing coming from BrC. While

7   these uncertainties in the aerosol direct effect are generally smaller than the uncertainties in

8   the forcing due to aerosol-cloud interactions (the indirect effect), they are still a significant

9   cause of differences between climate models.

10   Accurately accounting for the scattering and absorption of UV-VIS light by LAC aerosols is

11   thus critical for models of atmospheric composition, air quality, and climate change.

12   However, in order to reduce computational expense (so that the saved computational cycles

13   can be used to increase model resolution, number of chemical species, etc.), most global

14   chemical transport models (CTMs), such as the Global Modeling Initiative (GMI) Combo

15   model (Duncan et al., 2007) of the US National Aeronautics and Space Administration

16   (NASA) and GEOS-Chem (Bey et al., 2001), account for this absorption assuming that all

17   aerosol species are externally mixed (i.e., sulfate, sea salt, dust, OA, and black carbon

18   aerosols are not present in the same particle), and that each of these aerosol types have fixed,

19   prescribed size distributions. These simplifications can lead to substantial errors in simulating

20   the impact of LAC aerosols on photochemistry, as these impacts can vary substantially with

21   aerosol size and mixing state. For example, the studies of Liao et al. (1999) and Yang and

22   Levy (2004) showed that internal mixtures of sulfate and BC aerosols can cause larger

23   reductions of photolysis rates than external mixtures. Other theoretical (e.g., Jacobson, 2001)

24   and observational (e.g., Schwarz et al., 2008; Shiraiwa et al., 2010; Lack et al., 2012) studies

25   suggest that coatings on BC aerosol can enhance absorption by 30% or more. For example,

26   Kim et al. (2008) showed that accounting for internally-mixed aerosols and changing aerosol

27   size distributions with time gave a much smaller total negative TOA forcing (−0.12 W m^{-2}) of

28   all carbonaceous and sulfate aerosol compounds compared to the cases using one-moment

29   scheme either excluding or including internal mixtures (−0.42 and −0.71 W m^{-2},

30   respectively). However, core-in-shell Mie calculations carried out by Lack and Cappa (2010)

31   suggested that a black carbon particle coated with brown carbon can actually absorb less light

32   than a black carbon particle coated in non-absorbing material, with reductions in absorption of

33   up to 50% relative to clear coatings. In addition, Cappa et al. (2012) found little (~6%)

1   enhancement of BC absorption by coatings in California during the US Department of Energy

2   Carbonaceous Aerosols and Radiative Effects Study (CARES) in June of 2010. However,

3   these observations were made under dry conditions and thus the result may not apply at

4   higher RH.

5   Thus, while the simplifications used in the global CTMs greatly reduce the computational

6   expense of global studies of the impact of LAC aerosols on photochemistry, it is important to

7   quantify the errors in the simulation of aerosol scattering and absorption that result from the

8   assumption of an external mixture and the chosen size distributions for each aerosol type. In

9   situ closure studies, like the one in this work, allow the accuracy of the aerosol scattering and

10 absorption calculations in these models to be assessed independently of the potential errors in

11 other model processes such as the treatment of aerosol emission, secondary organic aerosol

12 (SOA) formation, and aerosol wet and dry deposition. In these closure studies, ambient

13 measurements of aerosol mass and composition are used as inputs to the aerosol optical

14 property routines of the global models, with the model-calculated aerosol optical properties

15 evaluated using simultaneous in situ measurements of aerosol scattering and absorption. In

16 addition, more detailed aerosol models that allow for time varying size distributions and more

17 complicated internal mixtures of aerosol, such as AER's Aerosol Simulation Program (ASP;

18 Alvarado, 2008; Alvarado and Prinn, 2009; Alvarado et al., 2015) can also be evaluated in

19 these closure studies to help determine if the errors in the global model routines are primarily

20 due to their fixed size distributions, assumptions about external mixtures, their assumptions

21 about the refractive indices of LAC, or interactions between these assumptions.

22 Previous closure studies have looked at both the scattering and absorption of aerosols

23 measured at surface sites (Sciare et al., 2005; Cai et al., 2011), from research vessels (Quinn

24 and Coffman, 1998) and from aircraft (Wex et al., 2002; Cai et al., 2011; Highwood et al.,

25 2012; Esteve et al., 2014). For example, Quinn and Coffman (1998) found agreement in the

26 submicron scattering calculated via a Mie code using the in situ size distribution and

27 composition measurements and measurements from an integrating nephelometer to within

28 measurement uncertainty, but did not get good agreement for supermicron aerosol. More

29 recently, Highwood et al. (2012) used a Mie code to simulate aerosol scattering (450, 550,

30 and 700 nm) and absorption (567 nm) for several aircraft flights during the EUCAARI-

31 LONGREX campaign, finding agreement within the measurement uncertainties of 30%.

32 Esteve et al. (2014) expanded on this work by using a flexible Mie code assuming

homogeneous internally mixed spheres. They found that the agreements between the calculation and measurements of absorption and scattering was within measurement uncertainties for EUCAARI-LONGREX, as in Highwood et al. (2012), but that there was poorer agreement for the VOCALS-Rex campaign, where detailed in situ observations of the aerosol size distribution were not available.

In this study, we evaluate four aerosol optical property parameterizations used in global models with in situ data on submicron aerosol scattering and absorption at three wavelengths (450, 550, and 700 nm for scattering, 470, 532, and 660 nm for absorption) gathered during the 2008 Arctic Research of the Composition of the Troposphere from Aircraft and Satellites (ARCTAS) campaign. The four parameterizations evaluated are from the Optical Properties of Aerosol and Clouds (OPAC v3.1; Hess et al., 1998) software package, the GMI Combo model, GEOS-Chem v9-02 (Bey et al., 2001), and the baseline configuration of a version of GEOS-Chem with online radiative transfer calculations (called GC-RT; Heald et al., 2014; Wang et al., 2014). This study differs from the closure studies discussed above in that these aerosol optical property modules, which simulate the aerosol as an external mixture of different components each with mixed size distributions, are evaluated directly without the additional constraints provided by the measured aerosol size distributions. We also use the ARCTAS data to perform the first evaluation of the aerosol optical property calculations in ASP v2.1, and investigate how the use of in situ size distribution information and the use of different mixing rules for BC affects the match with observations.

Section 2 describes the five aerosol optical property models examined in this study, including the ASP v2.1 model, while Section 3 describes the ARCTAS data used. Section 4 summarizes the methodology for the closure studies for both the global models (Section 4.1) and ASP v2.1 (Section 4.2). The results of the global model and ASP closure studies are discussed in Sections 5 and 6, respectively. The conclusions of the study and recommendations for future model development are summarized in Section 7.

2 Aerosol Optical Property Models

2.1 OPAC v3.1

The OPAC package was first described by Hess et al. (1998), and version 3.1 is available online at http://opac.userweb.mwn.de/radaer/opac-des.html#ftp. OPAC v3.1 includes microphysical and optical properties of six types of water clouds, three types of ice clouds and

1 ten aerosol types with size distributions and complex refractive indices chosen to represent

2 typical cases. The optical properties calculated include normalized extinction, scattering, and

3 absorption coefficients, single scattering albedo, asymmetry parameter, and the phase

4 function at 61 wavelengths between 250 nm and 40 μm for up to 8 values of relative

5 humidity. The aerosol components included are "water-insoluble" aerosols (primarily soil

6 particles), water-soluble aerosols (primarily organics and other secondary aerosol

7 components, see Hess et al., 1998), soot, two size modes of sea salt, four size modes of

8 mineral dust, and sulfate droplets. A given aerosol is then modeled as an external mixture of

9 these ten aerosol components. For the aerosol components analyzed in this paper (see Table

10 1), the optical properties are calculated from the assumed lognormal size distributions and

11 refractive indices using Mie theory.

12 2.2   NASA GMI Combo Model

13 The NASA GMI Combo model is a modular chemical transport model (Duncan et al., 2007;

14 Strahan et al., 2007; Bian et al., 2009) that includes treatment of both stratospheric and

15 tropospheric processes. Major atmospheric aerosol components included in the model are

16 sulfate, black carbon, OA, dust, and sea-salt using either GOCART (Chin et al., 2002, 2009;

17 Ginoux et al., 2001, 2004) or the University of Michigan/Lawrence Livermore National

18 Laboratory IMPACT model (Liu et al., 2007).

19 Within the NASA GMI Coupled model, the impact of aerosols on photolysis rates is

20 calculated using the FAST-JX model (v6.5). FAST-JX contains lookup tables of the

21 wavelength dependent extinction efficiencies, single scattering albedos, and phase function

22 coefficients for 14 aerosol types at 4 wavelengths (300, 400, 600, and 1000 nm) and at 7

23 values for relative humidity (0%, 50%, 70%, 80%, 90%, 95%, and 99%; see Supplement).

24 The 14 aerosol types include OA, black carbon, tropospheric, volcanic, and stratospheric

25 sulfate, two modes of sea salt, and seven modes of mineral dust. The optical properties in

26 these tables are based on Mie theory calculations (Mishchenko et al., 2002; Martin et al.,

27 2003), which were initially performed for GEOS-Chem. The relative humidity dependent

28 complex indices of refraction (calculated using a simple volume-average mixing rule, see

29 Hess et al., 1998) and lognormal size distributions are taken from the Global Aerosol Data Set

30 (GADS) of Köpke et al. (1997), which is in turn based on OPAC v3.1 except that (a) all

31 standard deviations of the modes are set to 2.0 and (b) the dry mode radius of sulfate used in

32 OPAC v3.1 (0.0695 μm) is reduced to 0.05 μm. FAST-JX then interpolates the aerosol

parameters contained in the look-up tables and calculates the average parameters for external mixtures of the aerosol types.

2.3 GEOS-Chem v9-02

The aerosol optical property parameterizations within GEOS-Chem v9-02 (Bey et al., 2001) follow a similar approach to the NASA GMI model, but the refractive indices and size distributions of several aerosol components have been updated based on the work of Wang et al. (2003a,b), Drury et al. (2010), and Jaegle et al. (2011). Table 1 shows the differences in the lognormal size distribution parameters, densities, and refractive indices for the aerosol types examined in this study from OPAC v3.1, GMI, GEOS-Chem v9-02, and the baseline configuration of GC-RT (discussed below). As in GMI, the optical properties for GEOS-Chem v9-02 are based on Mie theory calculations, but with changes to the assumed size distribution, refractive indices, and densities as noted in Table 1. In general, the geometric standard deviation of the size distribution σ used in GMI was reduced from the values of 2.0 to 1.6 for tropospheric sulfate, OA, and BC, and to 1.5 for the accumulation mode of sea salt. Furthermore, following Drury et al. (2010) the assumed geometric mean radius (r_g) of OA was increased by a factor of 3, the mean radius of BC was doubled, and the mean radius of sulfate was increased from 0.05 μm to 0.07 μm. Following Jaegle et al. (2011), the mean radius of the accumulation mode sea salt was reduced from 0.21 μm to 0.09 μm. The refractive index of tropospheric sulfate was also updated to reflect that of ammonium sulfate, rather than sulfuric acid aerosols.

2.4 Baseline GC-RT

GC-RT (Heald et al., 2014; Wang et al., 2014) is a configuration of GEOS-Chem that is coupled with the radiative transfer model RRTMG (Iacono et al., 2008) with modified aerosol optical properties relative to the standard GEOS-Chem code. Here we test the aerosol optical properties calculated by the "baseline" configuration of GC-RT described by Wang et al. (2014). As in GMI and GEOS-Chem v9-02, the optical properties in GC-RT are based on Mie theory calculations. The aerosol optical property calculation in the baseline configuration of GC-RT differs from GEOS-Chem v9-02 in that the BC density and refractive index are adjusted to the values recommended by Bond and Bergstrom (2006), which have been found to agree better with observations (Park et al, 2003; Stier et al, 2007; Kondo et al., 2011). These changes are shown in Table 1.

2.5 ASP v2.1

ASP (Alvarado and Prinn, 2009) simulates the gas-phase, aerosol-phase, and heterogeneous chemistry of young biomass burning smoke plumes, including the formation of O_3 and secondary inorganic and organic aerosol. ASP is a flexible, sectional size-resolved aerosol model that includes modules to calculate aerosol thermodynamics, gas-to-aerosol mass transfer (condensation/evaporation), coagulation of aerosols, and aerosol optical properties. ASP is generally run as a single box model, but it can be implemented as the chemistry subroutine of larger Eulerian and Lagrangian chemical transport models (e.g., Alvarado et al., 2009). ASP has been extensively used to study the chemical and physical transformations of aerosols within biomass burning smoke plumes and the optical properties of aerosols (Alvarado and Prinn, 2009; Alvarado et al., 2015) including the first simultaneous simulations of the fluid dynamics, radiative transfer, gas-phase chemistry, and aerosol-phase chemistry in a young biomass burning smoke plume (Alvarado et al., 2009). However, the aerosol optical property routines of ASP have not been previously evaluated with in situ data.

In this study we are using ASP v2.1 (Alvarado et al., 2015). The modules of ASP v2.1 most relevant to the current study are the modules for aerosol size distribution, thermodynamics, and optical properties. These modules are described in detail below.

2.5.1 ASP Aerosol Size Distribution

Aerosols are represented in ASP v2.1 as a single, internally-mixed moving-center sectional size distribution (Jacobson 1997, 2002, 2005). In this representation, size bin boundaries remain fixed while the mean particle size within the bin is allowed to change with time, and all particles in a size bin are assumed to have the same composition (except when the external mixture (EXT) mixing rule is used, see Section 2.5.2). In this study, the aerosol size distributions were modeled at a high resolution by using 40 size bins, 38 logarithmically distributed between diameters of 10 nm and 20 µm and one bin each for particles smaller than 10 nm or larger than 20 µm. Our tests found that increasing the number of bins used in ASP v2.1 to 100 changed the calculated optical properties by only ~1%. In ASP v2.1, the mass fractions of different aerosol components are assumed to be independent of aerosol size, so the relative aerosol composition is the same in each size bin. This assumption is likely to be violated for aerosols that contain significant amounts of BC (see Section 6.2), and is planned to be relaxed in future model development.

2.5.2 ASP Aerosol Optical Properties

As part of this work, we have extensively updated the calculations of aerosol optical properties within ASP v2.1 beyond those described by Alvarado (2008) and Alvarado and Prinn (2009). We have implemented spectrally-varying complex refractive indices for wavelengths between 250-700 nm for five aerosol components (H_2O, soot, sulfate, sea salt, and OA) based on those from OPAC v3.1 (Hess et al., 1998; see also Section 2.1 above). Similar to the procedure used in the NASA GMI Combo model and GEOS-Chem, we assume (1) that organics follow the OPAC v3.1 refractive indices of so-called "water-soluble particulate matter", (2) that all sulfate and nitrate salts follow the OPAC sulfate indices, (3) that all chloride salts follow the OPAC sea salt indices, and (4) that all BC follows the OPAC soot indices. The real refractive index of the inorganic aqueous solution (if present) is calculated using the molar refraction approach of Tang (1997) and Tang et al. (1997).

As in Alvarado and Prinn (2009), we assume here that all particles are spherical for the purposes of calculating their optical properties. ASP v2.1 has also been updated to include four mixing rules for the refractive indices of black carbon and the other aerosol components: (1) a volume-average (VA) dielectric constant mixing rule for all aerosol components; (2) a core-shell (CS) mixing rule, where a spherical core of BC is surrounded by a spherical shell of all other aerosol components (with the refractive index of the shell calculated using the volume-average dielectric constant mixing rule); (3) the Maxwell Garnett (MG) mixing rule, which here assumes that BC is present as a single randomly distributed inclusion within the particle (Maxwell Garnett, 1904); and (4) an external mixture (EXT) of BC and the other aerosols components, with both sets of particles having the same size distributions but with the relative number of particles determined by the relative volume concentrations. Mie calculations of aerosol optical properties for each bin of the size distribution are performed within ASP using the publicly available program DMiLay, which is based on the work of Toon and Ackerman (1981).

3 ARCTAS Data

The objective of the NASA ARCTAS campaign (Jacob et al., 2010) conducted in April and June-July 2008 was to better understand the factors driving current changes in Arctic atmospheric composition and climate. It used chemical and radiative measurements from three research aircraft (DC-8, P-3, B-200) to interpret and augment the continuous observations of Arctic atmospheric composition from satellites. The aircraft were based in

Alaska in April (ARCTAS-A) and in western Canada in June-July (ARCTAS-B). The focus of ARCTAS-A was to examine the long-range transport of anthropogenic pollution to the Arctic, while ARCTAS-B was more focused on the impacts of boreal forest fires on regional and global atmospheric composition. The summer ARCTAS-B deployment was preceded by one week of flights over California sponsored by the California Air Resources Board (CARB) to address regional issues of air quality and climate forcing.

Here we use data from the DC-8 aircraft during all three phases of ARCTAS, as described in detail below, to evaluate the aerosol optical property models. All analyses in this study used the "merged" data set averaged to the 10s time resolution of the Ultra-High Sensitivity Aerosol Spectrometer (UHSAS).

3.1 Aerosol Mass Concentrations and Composition

On the NASA DC8, submicron black carbon mass was measured with the University of Tokyo Single Particle Soot Photometer (SP2; Moteki and Kondo, 2007, 2008). The SP2 measures BC volume for particles with volume equivalent diameters between 90 nm and 1.0 μm. The measured BC volume is then converted to BC mass using an assumed density of 1.8 g/cm^3. The uncertainty in the BC mass measurements is ±30%. As a rough estimate, we calculate that by not measuring the BC mass below 90 nm, using the measured SP2 mass could bias a perfect absorption model low in absorption by about ~10%. However, as shown in Section 5 and 6, most models studied here overestimate submicron aerosol absorption, so this potential bias would tend to move the models closer to the observations. In addition, this bias is smaller than the potential bias in the absorption measurements due to the filter corrections, as noted in Section 3.3.

An Aerodyne high-resolution, time-of-flight aerosol mass spectrometer operated by the University of Colorado, Boulder (HR-ToF-AMS, hereafter AMS; DeCarlo et al., 2008; Cubison et al., 2011) was used to measure ammonium, chloride, nitrate, sulfate, and organic aerosol mass concentrations. The AMS primarily samples submicron aerosols, with 0% transmission for vacuum aerodynamic diameters below 35 nm and an approximate PM$_1$ size cut in vacuum aerodynamic diameter (DeCarlo et al., 2004; Canagaratna et al., 2007). The uncertainty of the AMS mass concentrations measurements (2σ) is ±34% for the inorganics and ±38% for the organics (Bahreini et al., 2009; Cubison et al., 2011), dominated by the

1 uncertainty in the particle collection efficiency due to particle bounce (e.g., Huffman et al.,
2 2005).

3 In addition, data on the concentration of water-soluble organic carbon (WSOC) in submicron
4 aerosol is provided by the Particle In Liquid Sampler (PILS-WSOC) of the Georgia Institute
5 of Technology (Sullivan et al., 2006), with an uncertainty of ±45%. The measured WSOC
6 was converted to total organic mass using a factor of 1.6. This value is uncertain to at least
7 ±0.4, but as our total OA concentration is determined by the AMS and the relative humidites
8 of the optical property measurements were low, this assumption has little impact on our
9 results. The PILS-WSOC data is used in the ASP closure study to separate water-soluble and
10 water-insoluble organic aerosol (see Section 4.2 below).

11 The AMS data were also supplemented with measurements of additional inorganic cations
12 from the University of New Hampshire Soluble Acidic Gases and Aerosol (UNH SAGA,
13 Dibb et al., 2003) instrument. SAGA collects non-size selected ("bulk"), isokinetically-
14 sampled aerosols onto a teflon filter. The ions are then extracted off the filter with deionized
15 water and analyzed via ion chromatography. In addition to the ions measured by the AMS,
16 SAGA provides measurements of the refractory cations sodium (± 0.1 ug/m^3 at 1013 hPa and
17 273.15 K), potassium (± 0.017 ug/m^3), magnesium (± 0.011 ug/m^3), and calcium (± 0.018
18 ug/m^3). In order to convert the SAGA bulk measurements of these ions into submicron
19 concentrations consistent with the AMS time-resolution, we use the bulk SAGA data to
20 determine a bulk ratio of these refractory cations to aerosol sulfate, and to combine these
21 ratios with the AMS measured sulfate concentrations to estimate the submicron mass
22 concentrations of the refractory cations.

23 To test this procedure, we compare AMS measured submicron nitrate, ammonium, and
24 chloride mass concentrations versus the concentrations estimated with the above SAGA-based
25 procedure. The match is very good for nitrate and ammonium (not shown), but submicron
26 chloride (not shown) is larger by the SAGA based procedure, as expected since SAGA is
27 sensitive to refractory chlorides such as NaCl and the AMS is not. However, as we expect the
28 aerosol in the ARCTAS campaign to be dominated by the species measured by the AMS and
29 the SP2, errors in our estimates of the submicron refractory cation mass should have little
30 impact on our closure study results.

3.2 Aerosol Size Distribution

In this study, we use the in situ measurements of dry aerosol size distribution provided by the instruments of the NASA Langley Aerosol Research Group (LARGE; Anderson et al., 1998). Specifically, we use the dry aerosol size distribution data from the TSI Scanning Mobility Particle Sizer (SMPS), the Droplet Measurement Technologies (DMT) Ultra-High Sensitivity Aerosol Spectrometer (UHSAS), and the TSI Aerodynamic Particle Sizer (APS) Model 3321.

The UHSAS is our primary source of size distribution information as the size range measured by the UHSAS (optical particle diameters between 60 nm to 1000 nm) measures the particles most likely to affect optical properties in the UV-VIS. The UHSAS has 99 bins geometrically distributed in this size range, and gathers data every 10 s. The estimated precision of the UHSAS is 5% in the particle size, and 20% in the particle number concentrations in each bin. Note that, as the UHSAS is an optical instrument, it can give incorrect size information if the refractive index of the particles is far from that of the polystyrene latex spheres used for calibration. This artifact can lead to a small underestimate of the size of submicron particles when it is not taken into account, thereby leading to an underestimate of scattering (e.g., Kassianov et al., 2015). However, we expect that this effect on our study will be small relative to the stated precision of the UHSAS.

The TSI SMPS measures dry aerosol size distributions in 54 size bins with geometric diameters between 8.8 nm and 399.7 nm. The time resolution is lower than the UHSAS (105s for the SMPS versus 10 s for the UHSAS), and so care has to be taken in matching SMPS size distributions with the UHSAS, as described in Section 4.2. The estimated precision of the SMPS is 5% in the particle size, and 25% in the particle number concentrations in each bin.

The TSI APS measures dry aerosol size distributions in 13 size bins with aerodynamic diameters between 0.583 μm and 7.75 μm. The time resolution is the same as the UHSAS, but the measured diameters are different (optical diameter for the UHSAS, aerodynamic diameter for the APS). Converting continuum-regime aerodynamic diameter D_{aero} to geometric diameter D_{geo} is done through the equation:

$$D_{geo} = D_{aero}\sqrt{\frac{X}{\rho}}. \qquad (3)$$

where ρ is the particle density and X is the "dynamic shape factor" that accounts for the non-sphericity of the particles (for spheres, $X = 1.0$, otherwise $X > 1$). The estimated precision of

1 the APS is 10% in the particle size, and 20% in the particle number concentrations in each
2 bin.

3.3 Aerosol Optical Properties

In this study, we use the in situ measurements of dry aerosol scattering and absorption provided by the LARGE suite of instruments. During ARCTAS, LARGE measured dry total aerosol scattering and hemispherical backscattering coefficients at three wavelengths (450 nm, 550 nm, and 700 nm) using a TSI model 3563 nephelometer with an estimated precision of 0.5 Mm^{-1}. These total scattering coefficients were then corrected for truncation errors using the procedure described by Anderson and Ogren (1998), who report a measurement reproducibility of ±1%. Thus the actual uncertainty in the scattering meaurements is ±1% or ±0.5 Mm^{-1}, whichever is larger. A Radiance Research (RR) nephelometer with a 1 μm cut cyclone measured the scattering of submicron aerosols at 532 nm. This data allowed an estimate of the submicron scattering at 450nm, 550 nm, and 700 nm by comparison of the two nephelometers when they were sampling mainly submicron particles (i.e., a fine mode fraction > 0.6).

Dry total and submicron absorption was also measured at three wavelengths (467 nm, 532 nm, and 660 nm) using a RR Particle Soot Absorption Photometer (PSAP) with an estimated precision of 0.2 Mm^{-1}. These filter-based absorption measurements were corrected to in situ values using two methods: one from Virkkula (2010) and one from Lack et al. (2008). These two corrections can differ by about 20-30%, with Virkkula (2010) giving lower aerosol absorption. Thus the practical uncertainty in the absorption measurement is estimated as at least 20-30%. Most of our analysis is based on the correction of Lack et al. (2008), but we discuss the sensitivity of our conclusions to the choice of correction as well. The PSAP submicron absorption measurement is well correlated with the submicron BC mass (not shown), with an overall r^2 of 0.64, but the data is uncorrelated for low BC mass concentrations (<0.03 μg m^{-3}), which occurs for 261 out of 10,356 data points in our absorption analysis. However, as we have no clear evidence that these PSAP data points are incorrect and excluding them does not appreciably change the conclusions of our study, we have included these data points in our analysis below.

1 **4 Closure Study Methodology**

2 **4.1 Fixed Size Distribution Parameterizations**

3 As OPAC, GMI, GEOS-Chem, and GC-RT all share a common heritage and features (i.e.,

4 external mixtures of fixed size distributions of the various aerosol components) our closure

5 study methodology for all four parameterizations is also similar. The general procedure is

6 shown in Figure 1a. The first step is to assign the measured aerosol mass concentrations to the

7 different aerosol types. In this study we focus on tropospheric, submicron aerosol, as detailed

8 composition data is available from the AMS and SP2 for this size range, and thus we exclude

9 the mineral dust, stratospheric sulfate, volcanic sulfate, and coarse mode sea salt aerosol

10 types. The SP2-measured submicron mass of BC is assigned to the BC (for GMI, GEOS-

11 Chem, and GC-RT) or SOOT (for OPAC) aerosol types. The AMS-measured submicron OA

12 mass is assigned to the OA (for GMI, GEOS-Chem, and GC-RT) or WASO (for OPAC)

13 aerosol types. For the inorganic species measured by the AMS and SAGA, we calculate

14 "equivalent electrolytes" consistent with the measured and estimated submicron ion

15 concentrations (see Equation 17.72 of Jacobson, 2005). The sulfate- and nitrate-containing

16 electrolytes are then assigned to the tropospheric sulfate (for GMI, GEOS-Chem, and GC-RT)

17 and SUSO (for OPAC) aerosol types, while the chloride-containing electrolytes are assigned

18 to the accumulation mode sea salt type.

19 The second step involves determining the submicron scattering coefficient, absorption

20 coefficient, single scattering albedo (SSA), and asymmetry parameter for each aerosol type at

21 the measured wavelengths and relative humidities (RHs). This is done through linear

22 interpolation of the values present in the look-up tables for each aerosol parameterization. As

23 the LARGE instruments measure dry optical properties, the RH used in the interpolation

24 should not be the ambient RH, but instead is the RH in the inlet prior to the measurement.

25 Here, we used the measured inlet RH in all comparisons. This "dry" RH is generally near 0%,

26 but can get as high as 20%.

27 For GMI, GEOS-Chem, and GC-RT, the tabulated properties include the extinction efficiency

28 (Q_{ext}), effective radius (r_{eff}), and SSA (ω) for each aerosol type j. After correction for

29 wavelength and RH as described above, the volume extinction coefficient ($k_{ext,j}$) for each

30 aerosol type is calculated from these properties by the equation:

1 $$k_{ext,j} = \frac{3}{4} \frac{Q_{ext,j}}{r_{eff,j}} \frac{m_j}{\rho_j}. \tag{4}$$

2 where m_j is the mass concentration for each aerosol type ($\mu g/m^3$, corrected to ambient

3 temperature and pressure) and ρ_j is the particle density. The scattering and absorption

4 coefficients are then calculated as $k_{scat,j} = \omega_j k_{ext,j}$ and $k_{abs,j} = (1-\omega_j)k_{ext,j}$. The k_{ext}, k_{scat}, k_{abs},

5 and ω for each aerosol type are then combined together to give the model estimate of the

6 optical properties for the submicron aerosol mixture. For k_{ext}, k_{scat}, and k_{abs} this is a simple

7 sum, e.g. $k_{scat} = \sum_j k_{scat,j}$, and ω is the ratio of k_{scat} to k_{ext}.

8 For OPAC, the tabulated properties include values of $k_{ext,j}$, $k_{scat,j}$, $k_{abs,j}$, and ω_j, with $k_{ext,j}$, $k_{scat,j}$,

9 and $k_{abs,j}$ normalized to an assumed particle number concentration of 1 cm^{-3}. These normalized

10 values are multiplied by the ratio of the measured mass concentration m_j to the assumed mass

11 concentration for 1 particle cm^{-3} for each aerosol type. These properties are then corrected for

12 wavelength and RH and combined together as described above for the GMI and GEOS-Chem

13 parameterizations.

14 **4.2   ASP v2.1**

15 The ASP v2.1 model closure studies (see Figure 1b) differ from the other closure studies

16 mainly in the use of the data on the in situ dry aerosol size distribution from the LARGE

17 instrument suite. As noted in Section 3.2 above, this data comes from three different

18 instruments (the SMPS, UHSAS, and APS) with different time resolutions and measuring

19 techniques. Thus combining these observations into a consistent picture of the size

20 distribution is not a straightforward task. Our approach uses the UHSAS observations as the

21 core of our size distribution estimate, as the submicron aerosol optical properties of interest

22 here are likely most sensitive to aerosol within the size range of the UHSAS (60 nm – 1000

23 nm). We start by creating a "combined" size distribution with the same size resolution as the

24 UHSAS observations, but with an expanded range (i.e., 246 bins with optical diameters

25 between 8.8 nm and 10 µm). For size bins with diameters between 60 nm and 850 nm, the

26 UHSAS data is used directly. For size bins below 60 nm, SMPS data (interpolated to the

27 UHSAS size resolution) is used. As the SMPS has a lower time resolution than the UHSAS,

28 we scale the SMPS data to match the UHSAS data in the size range 60 nm to 100 nm – the

29 scale factor is the slope of the linear regression of the (interpolated) SMPS and UHSAS data

1   in this size range. For size bins larger than 850 nm, the size distribution is based on the APS

2   data, with the conversion factor between aerodynamic and geometric diameter assumed to be

3   0.8. This value is consistent with the density and shape factors of urban aerosols and solid

4   ammonium sulfate (Reid et al., 2006), and for a spherical particle is equivalent to a density of

5   1.56 g cm^{-3}. The corrected APS data is used to define a power law that describes how the size

6   distribution decays at optical diameters larger than 850 nm, and this power law is used to

7   extrapolate the UHSAS data for diameters larger than 850 nm.

8   While ASP v2.1 represented the aerosol as a sectional size distribution as described in Section

9   2.5.1, the initialization routines of ASP v2.1 require that the dry aerosol size distributions be

10 input as a sum of lognormal modes which are then used to populate the size bins. Thus the

11 "combined" size distribution described above is fit to three lognormal modes (see Equations

12 13.18 and 13.20 from Jacobson, 2005). The fitting boundaries for the three modes are fixed at

13 8 – 80 nm, 80 – 400 nm, and 400 nm – 10 μm, as these boundaries coincide with minima in

14 the ARCTAS size distribution data.

15 The submicron aerosol mass concentrations of BC, OA, and equivalent electrolytes were

16 calculated as described in Section 4.1. OA was assumed to be fairly involatile and was

17 assigned to the species CBIO (if water-soluble) and POA1 (if not water soluble; Alvarado,

18 2008). These mass concentrations define the relative mass composition (i.e. mass fractions) in

19 the ASP modes. This aerosol composition was assumed to be the same for all three modes

20 input to ASP v2.1 – while the AMS can be used to obtain size-resolved composition, the

21 averaging times required for this data are large (about an hour), and thus are not useful for

22 comparison to the 10 s resolution optical property data. This implicitly assumes that the size

23 distributions of all aerosol components (BC, OC, and electrolytes) are the same, which may

24 not have been true in the ambient atmosphere.

25 We then used ASP v2.1 to calculate total and submicron k_{scat}, k_{abs}, and ω for wavelengths

26 between 250 nm and 700 nm (at 1 nm resolution) using each of the four mixing rules

27 described above: volume-averaged, core-shell, Maxwell-Garnett, and external mixture. These

28 were compared with the in situ measurements of optical properties from the LARGE

29 instruments.

5 Fixed Size Distribution Parameterization Results

5.1 Scattering

Figure 2 shows a scatterplot of the measured submicron scattering coefficient at 550 nm versus the value calculated using the optical property tables of the GMI Combo model. The slope and correlation coefficient (r^2) of a linear fit to the data from the entire ARCTAS campaign are used in evaluating the models; these values are summarized in Table 2. We see that all four parameterizations explain 70-74% of the variability (e.g., r^2 = 0.70-0.74) in the observed submicron scattering at all three wavelengths, except for the GMI model at 700 nm, where only 58% of the variability is explained. The slopes of the linear fits are between 0.89 and 1.08 for the 450 and 550 nm channels, but the 700 nm channel shows more variability, with a slope of 1.19 for OPAC v3.1 and the slopes for the other models between 0.63-0.68.

However, Figure 2 shows that there can be substantial differences in the results for the different phases of the ARCTAS campaign. The parameterizations generally work best for the ARCTAS-B campaign, which sampled several fresh biomass-burning plumes and thus likely had more externally mixed aerosol samples than the other two phases that sampled more aged pollution. For ARCTAS-B the r^2 values were ~0.75, with slopes between 0.99 and 1.15. In contrast, the models generally overestimate the relatively smaller scattering coefficients of the aged arctic pollution sampled during the ARCTAS-A campaign, with r^2 values of ~0.63 and slopes between 1.5 (OPAC v3.1) and 2.0 (GEOS-Chem v9-02). The ARCTAS-CARB phase shows a clear bifurcation, with some samples overestimated by a factor of 2 or more and some underestimated by similar factors, suggesting two distinct types of aerosols were sampled in this phase. This leads to poor r^2 values for this phase (0.25-0.39) and, as the largest values are generally underestimated, slopes between 0.40 (OPAC v3.1) and 0.70 (GEOS-Chem v9-02).

We also examined the distribution of the errors (modeled value – measured value) of the submicron scattering coefficient, as shown in Figure 3 for 550 nm and the GMI model. To reduce the impact of the large dynamic range of the measured scattering coefficients on our analysis, we examined the errors in the logarithm (base 10) of the scattering coefficients, which is equivalent to the logarithm of the ratio of the modeled to measured value. The mean (μ) and standard deviation (σ) of these error distributions are also summarized in Table 2. We prefer these metrics over mean normalized bias (MNB), as with the logarithmic (geometric)

18

1   approach an overestimate of a factor of 2 and an underestimate of a factor of 2 average out to

2   no mean error, while the MNB of these two observations would be 25% due to the asymmetry

3   of overestimates and underestimates when expressed as percentages. However, the use of

4   MNB instead of μ does not substantially alter the conclusions of our study, and values for

5   MNB are also discussed below.

6   The spread of the errors is very similar for all models and wavelengths, with σ of ~0.25,

7   which is equivalent to a standard deviation of a factor of 1.8 about the mean. The histograms

8   of the errors show little skew to either side of the mean value. The models give a positive bias

9   at 450 and 550 nm (see Table 2), with the GMI model having the lowest mean bias in these

10 channels (μ = 0.06 and 0.09, respectively, equivalent to a geometric mean overestimate of

11 15% and 23%, and an MNB of 35% and 46%). As the 450 nm channel is closest to the UV

12 wavelengths important in photolysis, we would thus expect the GMI model to perform best in

13 modeling the impact of aerosols on photolysis rates. GEOS-Chem v9-02 has a slightly smaller

14 negative bias (-0.04, equivalent to a geometric mean underestimate of 9% and an MNB of

15 8.5%) than GMI (μ = -0.05, geometric mean underestimate of 11%, MNB of 16%) in the 700

16 nm channel. The results for GC-RT are similar to GEOS-Chem v9-02 at 450 and 550 nm, but

17 the negative bias at 700 nm is about twice as large on average in GC-RT as it is in GMI or

18 GEOS-Chem v9-02.

19 In order to interpret these closure study results, it is useful to estimate the values of μ and σ

20 we would expect from a perfect model based on the uncertainty in the input mass

21 concentrations and the uncertainty in the scattering measurement. Taking the sum of the

22 squares in the relative standard errors in the mass concentrations of OA (19%), sulfate (17%),

23 nitrate (17%), ammonium (17%), chloride (17%), and BC (30%), as well as the estimated

24 nephelometer uncertainty (1%) gives an overall uncertainty estimate of ±49%, corresponding

25 to a σ of 0.17. Thus even a perfect model would have a fairly significant spread in it's

26 histogram of errors. However, as we are using ~10,000 data points in our comparison, the

27 expected error in μ is about a factor of 100 lower, and thus we would expect $|\mu| \ll 0.01$.

28 **5.2   Absorption and SSA**

29 Figure 4 shows a scatterplot of the measured submicron absorption coefficient at 532 nm

30 versus the value calculated using the optical property tables of the GMI model. The PSAP

31 measurements have been corrected using the approaches of Lack et al. (2008) (Figure 4a) and

1   Virkkula (2010) (Figure 4b). As stated in Section 3.3 above, the Virkkula (2010) correction

2   generally gives 20-30% lower aerosol absorption coefficients than the Lack et al. (2008)

3   correction. As the models tended to overestimate aerosol absorption using both corrections,

4   we discuss our results relative to the Lack et al. (2008) corrected values. Results for all

5   model-wavelength combinations using the Lack et al. (2008) correction are summarized in

6   Table 3. Unlike for scattering, the absorption coefficient slopes and correlations are fairly

7   consistent between the ARCTAS-B and ARCTAS-CARB phases of the campaign, but the

8   ARCTAS-A phase shows larger model overestimates of aerosol absorption for the aged

9   Arctic pollution sampled in that campaign. The global model parameterizations can explain

10   65-72% of the observed variability, comparable to but a little worse than their performance

11   for scattering (see Section 5.1), with slopes between 0.75 (GMI, 660 nm) and 1.21 (GEOS-

12   Chem v9-02, 532 nm).

13   Figure 5 shows the histogram of the errors in the logarithm of the submicron aerosol

14   absorption coefficient for GMI at 532 nm, while the mean and standard deviation for all

15   model-measurement combinations are summarized in Table 3. The expected values of μ and

16   σ from a perfect model are $\ll 0.01$ and ~ 0.20, respectively, reflecting the input uncertainties

17   discussed for scattering in Section 5.1 as well as the ~30% uncertainty in converting the filter-

18   based PSAP measurement to the ambient absorption. The spread of the errors (measured by

19   the standard deviation σ) is between 0.24-0.29 for all model-wavelength combinations, giving

20   a standard error of a factor of ~1.7 to 2.0 around the mean bias. We can see that while all the

21   models show a positive mean bias for aerosol absorption at all wavelengths, the GMI model

22   has the smallest mean bias at all wavelengths, with a maximum bias at 532 nm ($\mu = 0.06$, or a

23   15% geometric mean overestimate, and an MNB of 39%). Similar results hold when the

24   Virkkula (2010) correction is used, but the geometric mean overestimate for GMI at 532 nm

25   increases to 55%. Thus while we can conclude the GMI parameterization performs the best

26   for submicron aerosol absorption of the global model parameterizations evaluated in this

27   study, we can only conclude that its geometric mean error is within the range of 0-55%,

28   depending on wavelength and PSAP correction. Table 3 also shows that the mean

29   overestimate in aerosol absorption in GEOS-Chem v9-02 has been substantially reduced, but

30   not eliminated, by the improved values for BC density and refractive index in GC-RT (e.g.,

31   from $\mu = 0.27$ and MNB of 120% in GEOS-Chem v9-02 to $\mu = 0.22$ and MNB of 95% in GC-

32   RT at 532 nm), and the correlation coefficients are slightly improved as well.

1   Figure 6 shows the results for Single Scattering Albedo (SSA) for the GMI model at 550 nm.

2   The Lack et al. (2008) measured absorptions at 532 nm and 660 nm were used to derive an

3   absorption Angstrom exponent that was then used to estimate the observed absorption at 550

4   nm. As expected, since both the GMI scattering and absorption comparisons showed small

5   positive biases at this wavelength (see Tables 2 and 3), the GMI calculation of SSA is

6   relatively unbiased, as shown in Table 4. However, the spread of the errors is large ($\sigma = 0.05$),

7   and the correlation between the modeled and measured values is poor ($r^2 = 0.06$). Note that

8   the size of the uncertainties in SSA seen in Table 4 can have a significant impact on estimates

9   of global aerosol DRF. For example, Loeb and Su (2010) found that a SSA perturbation of

10 0.03 over land and 0.06 over ocean could lead to errors in all-sky DRF of -0.73 to +1.11 W m^{-}

11 ^{2}.

12 We explored whether averaging the observations at 1 and 5 minute intervals would reduce the

13 spread in the SSA errors and improve the correlation. However, the spread of errors only

14 decreased to $\sigma = 0.03$ when the data is averaged to 5 minute intervals, and the correlation

15 coefficient only increased to $r^2 = 0.22$. Thus, while the GMI model gives reasonable mean

16 values for SSA, the calculated value tends to be significantly wrong for any given data point.

17 In addition, the GEOS-Chem v9-02 and GC-RT SSA predictions show similar biases and

18 spread of errors, with GC-RT performing slightly better than the other models at 450 nm.

19 **6   ASP v2.1 Results**

20 **6.1   Impact of Size Distribution Data on Aerosol Scattering**

21 As expected, when ASP v2.1 is given aerosol size distribution data from the LARGE

22 instrument suite, it does a substantially better job of modeling the observed aerosol scattering

23 than the global model parameterizations discussed in Section 5.1. Figure 7 shows the

24 scatterplot and histogram of the errors in submicron aerosol scattering for ASP v2.1 at 550

25 nm. The results for a core-shell (CS) BC mixing rule are shown, but the results for all other

26 mixing rules are similar, as shown in Table 5. Note that there are far fewer data points in

27 Figure 7a than in Figure 2 for the GMI model (1,771 versus 10,629). This is because the ASP

28 v2.1 closure requires all three LARGE size distribution instruments to be working at the same

29 time as the AMS, SP2, and other composition instruments, which reduces the amount of

30 available data. With the size distribution data, ASP v2.1 with the core-shell mixing rule is

31 able to explain 88-89% of the observed variability in aerosol scattering, with linear regression

1   slopes of 0.99, 1.00, and 1.07 at 450, 550, and 700 nm, respectively. The maximum mean

2   (logarithmic) bias is μ = -0.03 (equivalent to a mean underestimate of 7%), and the standard

3   deviation of the logarithmic errors (σ) is only 0.17, equivalent to a factor of 1.5. Given that

4   the size distribution data is itself uncertain to 20% before the instruments are stitched

5   together, this is remarkably good model performance - we estimate that a perfect model

6   would have a σ of 0.13 due to the uncertainty in the size distributions and the relative mass

7   contributions. Together this implies that ASP v2.1 is able to model more than 90% of the

8   scattering data points to within a factor of 2.

9   **6.2   Impact of Size Distribution Data and Black Carbon Mixing Rule on Aerosol**

10   **Absorption**

11   In contrast to the results for scattering, ASP v2.1, with aerosol size distribution data from the

12   LARGE instrument suite, has difficulty reproducing the observations for aerosol absorption.

13   Figure 8a shows a scatterplot of the measured submicron absorption coefficient versus the

14   value calculated by ASP v2.1 using a CS mixing rule. While overall slope (0.93 ± 0.12) is

15   reasonable, there are clear problems in the simulation of the absorption observations from

16   ARCTAS-B and CARB, leading to a poorer correlation coefficient (r^2 = 0.44) and a larger

17   spread in the errors (σ = 0.32, see Figure 8b) than was seen for the global parameterizations

18   using fixed size distributions and external mixtures. We estimate that a perfect model would

19   have a σ of 0.17 due to the uncertainty in the size distributions, the relative mass

20   contributions, and in the absorption measurement.

21   Table 6 summarizes the submicron absorption results averaged over all ARCTAS phases for

22   the different BC mixing rules that can be used in ASP v2.1. The relatively poor correlation

23   and wide spread of errors is consistent across mixing rules. As expected, the assumption of an

24   external mixture (EXT) results in the lowest modeled absorption, significantly

25   underestimating absorption at 470 nm and 532 nm, but giving very little bias at 660 nm. In

26   contrast, the internal mixtures (CS, MG, and VA) all overestimate absorption, but show much

27   less dependence of this bias on wavelength. CS and VA both give regression slopes near 1,

28   but the VA mixing rule shows a larger overestimate of absorption than the CS mixing rule,

29   while the MG mixing rule has a lower positive bias than CS.

30   However, the results vary significantly between the different phases of ARCTAS. For

31   example, Figure 9 shows the histograms of the ASP errors when the CS mixing rule is used

1 separated for the three campaigns. We can see that both the mean bias and the spread of the
2 errors vary significantly between the campaigns. For example, ASP with CS appears
3 relatively unbiased for ARCTAS-CARB (μ = -0.02) but the spread of the errors is large (σ =
4 0.36). The results for ARCTAS-A show a small positive bias (μ = 0.07) similar to the overall
5 GMI results (μ = 0.06, see Table 3), but with a small spread in the errors (σ = 0.18). In
6 contrast, ASP with CS substantially overestimates absorption during ARCTAS-B by an
7 average factor of 2 (μ = 0.32), but again shows a relatively small spread of errors (σ = 0.23).

8 These differences between the campaigns make sense when we consider the types of pollution
9 sampled during each campaign. ARCTAS-A sampled primarily aged Arctic haze particles,
10 and so the BC in these particles would be expected to be internally mixed. In contrast,
11 ARCTAS-B sampled substantial amounts of fresh biomass burning smoke, where about half
12 of the BC would be expected to be externally mixed (e.g., Akagi et al., 2012) and thus have
13 lower absorption per mass of BC than would be calculated by the core-shell assumption.
14 Finally, ARCTAS-CARB sampled a mixture of anthropogenic pollution and biomass burning
15 smoke from a variety of sources. These aerosols are likely in a variety of mixing states and
16 have a variety of size distributions of BC particles, and thus ASP CS would be expected to
17 show the large spread of errors seen. These results do not definitively prove that the
18 difference in the performance of ASP v2.1 for the three ARCTAS campaigns is due to errors
19 in mixing state, but they do suggest the need for further development of the ASP model to
20 allow for time-varying mixing states and to allow the BC size distribution to vary
21 independently of the overall size distribution.

22 In order to examine the benefit that including a time-varying mixing state for BC in ASP
23 could bring, we examined a third "variable" mixing rule case where CS was used for
24 ARCTAS-A and ARCTAS-CARB while EXT was used for ARCTAS-B. The results are
25 shown in Figure 10 and Table 6. This variable mixing rule generally shows lower mean
26 positive biases than any of the internally-mixed rules (CS, VA, MG) while showing a slightly
27 smaller spread in the errors than any of the constant mixing rule cases (σ of 0.28-0.29 versus
28 0.30-0.32), more consistent with the GMI results seen in Table 3. However, the correlation
29 coefficient is still very poor (r^2 = 0.44-0.45), suggesting that the assumption in ASP v2.1 of a
30 constant mixing ratio of BC throughout the overall size distribution can lead to errors in
31 submicron aerosol absorption as large as those seen in the externally-mixed, fixed-size
32 distribution global models.

Table 7 summarizes the results for SSA for ASP v2.1 using different mixing rules. When assuming internal mixtures, ASP tends to underestimate the SSA by an average of 0.01 to 0.04, while assuming external mixtures gives fairly unbiased results (-0.01 to 0.01). We see that the "variable" mixing rule gives small negative biases similar to the results from the MG mixing rule, but has a higher correlation coefficient (r^2 of 0.30 at 532 nm, compared to 0.20 for MG). The SSA correlation coefficients for ASP v2.1 for all mixing rules are generally higher than those for GMI or GEOS-Chem v9-02.

7 Conclusions

We performed a closure study using in situ observations of submicron aerosol concentration, composition, size distribution, scattering, and absorption from the NASA ARCTAS campaign to evaluate the modeling of submicron aerosol scattering and absorption in four global parameterizations (those used in the GMI Combo model, OPAC v3.1, GEOS-Chem v9-02, and the baseline configuration of GC-RT) as well as the smoke plume chemistry model ASP v2.1. Our closure study allowed for the evaluation of the predictions of aerosol scattering and absorption by these models without the complications associated with different treatments of aerosol emissions, transport, chemistry, and deposition. We find that the GMI model has smaller mean biases in predicting submicron aerosol scattering and absorption than OPAC v3.1, GEOS-Chem v9-02, or the baseline GC-RT. The better performance of GMI for absorption seems to be primarily due to the assumption of a larger density for BC (1.5 g cm^{-3}) than in OPAC v3.1, as the size distribution and refractive index for BC are the same for these models. On average, GMI overestimates submicron aerosol scattering during ARCTAS by 15% (1σ range -34% to 100%) at 450 nm and 23% (-29% to 114%) at 550 nm, while it underestimates scattering at 700 nm by -11% (-53% to 66%). When the Lack et al. (2008) correction is applied to the ARCTAS PSAP observations, GMI overestimates submicron aerosol absorption by 10% (1σ range -41% to 104%) at 470 nm, by 15% (-38% to 114%) at 532 nm, and by 0% (-42% to 74%) at 660 nm. On average GMI slightly overestimates mean submicron SSA during ARCTAS (0.01 ± 0.05 at 470 and 532 nm, 0.02 ± 0.07 at 660 nm) while GEOS-Chem v9-02 slightly underestimates it (-0.01 ± 0.05 at 470 and 532 nm, -0.02 ± 0.06 at 660 nm), but the correlation is very poor for all models, suggesting that while the mean is reasonable the models tend to have little skill predicting individual data points. We also find that the changes to the treatment of BC in the baseline configuration of GC-RT reduce the positive bias in modeled absorption relative to that in GEOS-Chem v9-02 (e.g.,

24

1 from a mean overestimate of 86% in GEOS-Chem v9-02 to a mean overestimate of 66% at

2 532 nm). This is likely due to a net reduction in BC absorption due to the increase in the

3 assumed density of BC (1.0 g cm^{-3} in GEOS-Chem v9-02, 1.8 g cm^{-3} in GC-RT) that is

4 partially offset by the increased imaginary refractive index for BC in GC-RT.

5 The use of in situ size distribution information allows ASP v2.1 to accurately simulate

6 submicron aerosol scattering with a high correlation (r^2 = 0.88-0.89) and very little spread in

7 the error distribution compared to the GMI model. When a core-shell (CS) BC mixing rule is

8 used, ASP v2.1 underestimates aerosol scattering during ARCTAS by 7% (1σ range -37% to

9 38%) at 450 and 550 nm and 2% (-34% to 45%) at 700 nm on average. However, the ASP

10 v2.1 results for submicron aerosol absorption show a substantially lower correlation (r^2 =

11 0.44-0.50) likely due to the assumption in ASP v2.1 of a constant mass fraction of BC

12 throughout the size distribution. When a CS mixing rule is used, ASP v2.1 overestimates

13 submicron aerosol absorption by 29 to 35% with a weak dependence on wavelength, while

14 ASP v2.1 with an external (EXT) mixture in ASP tends to underestimate aerosol absorption,

15 with the average errors showing a strong dependence on wavelength (-21% at 470 nm, -11%

16 at 532 nm, and 0% at 660 nm). Examination of the distribution of errors for each phase of the

17 ARCTAS campaign suggests that an external mixture is best for the fresh smoke observations

18 in ARCTAS-B, while an internally mixed core-shell approach is better for the aged Arctic

19 haze in ARCTAS-A and the anthropogenic pollution in ARCTAS-CARB. Using this

20 "variable" mixing rule in ASP v2.1 leads to an average overestimate of aerosol absorption of

21 10% (1σ range -42% to 109%) at 470 nm, 17% (-38% to 124%) at 532 nm, and 23% (-37% to

22 140%) at 660 nm.

23 These results suggest that the GMI model performs the best of the four fixed size distribution

24 schemes evaluated here in simulating submicron aerosol scattering and absorption, and that

25 future refinements to the GMI approach should focus on improvements that, on average,

26 reduce scattering and absorption in the 550/532 nm and 450/470 nm bands. Increasing the

27 density of OC in GMI to 1.8 g cm^{-3} to match the other fixed-sixe distribution models would

28 likely reduce all three wavelengths equally, and the changes to the fixed size distribution

29 parameters examined here generally resulted in stronger absorption and scattering in all

30 wavelengths, so refining the wavelength dependence of the complex refractive indices used in

31 GMI might be the most promising pathway for significant improvements. For GEOS-Chem,

32 adopting the baseline GC-RT BC parameters from Wang et al. (2014) for the standard GEOS-

Chem model would substantially improve the ability of the model to simulate aerosol absorption. However, further refinements to the treatment of BC and OA absorption are needed to reduce the positive bias that remains in GC-RT, such as the potential of BrC absorption to decrease with atmospheric age (e.g., Forrester et al., 2015). For ASP v2.1, the results show that future model development should focus on improvements to the simulation of submicron aerosol absorption by adding routines that allow for a more complete description of aerosol mixing state (such as in the PartMC-MOSAIC model, Tian et al., 2014) and adding the ability for the BC mass fraction to vary with aerosol size. In addition, similar closure studies should be performed with data from other recent field campaigns, such as NASA Studies of Emissions and Atmospheric Composition, Clouds and Climate Coupling by Regional Surveys (SEAC[4]RS; Toon, 2013) and the US Department of Energy Biomass Burning Observation Project (BBOP; Kleinman et al., 2014) campaign, to investigate how the biases in the aerosol optical property models vary with location and pollution source.

Acknowledgements

1 **References**

2 Alvarado, M. J.: Formation of Ozone and Growth of Aerosols in Young Smoke Plumes from

3 Biomass Burning, Ph.D. Thesis, Massachusetts Institute of Technology, Cambridge, MA,

4 USA, 324 pp., available at http://globalchange.mit.edu/files/document/

5 Alvarado_PhD_08.pdf, 2008.

6 Alvarado, M. J. and Prinn, R. G.: Formation of ozone and growth of aerosols in young smoke

7 plumes from biomass burning: 1. Lagrangian parcel studies, J. Geophys. Res., 114, D09306,

8 doi:10.1029/2008JD011144, 2009.

9 Alvarado, M. J., Wang, C., and Prinn, R. G.: Formation of ozone and growth of aerosols in

10 young smoke plumes from biomass burning: 2. Three-dimensional Eulerian studies, J.

11 Geophys. Res., 114, D09307, doi:10.1029/2008JD011186, 2009.

12 Alvarado, M. J., Lonsdale, C. R., Yokelson, R. J., Akagi, S. K., Coe, H., Craven, J. S.,

13 Fischer, E. V., McMeeking, G. R., Seinfeld, J. H., Soni, T., Taylor, J. W., Weise, D. R., and

14 Wold, C. E.: Investigating the Links Between Ozone and Organic Aerosol Chemistry in a

15 Biomass Burning Plume from a Prescribed Fire in California Chaparral, Atmos. Chem. Phys.,

16 15, 6667–6688, doi:10.5194/acp-15-6667-2015, 2015.

17 Anderson, B. E., Cofer, W. R., Bagwell, D. R., Barrick, J. W., Hudgins, C. H., Brunke, K. E.:

18 Airborne observations of aircraft aerosol emissions 1: total nonvolatile particle emission

19 indices, Geophys. Res. Lett., 25, 1689–1692, 1998.

20 Anderson, T. L. and Ogren, J. A.: Determining Aerosol Radiative Properties Using the TSI

21 3563 Integrating Nephelometer, Aerosol Science and Technology, 29, 57–69,

22 doi:10.1080/02786829808965551, 1998.

23 Andreae, M. O. and Gelencsér, A.: Black carbon or brown carbon? The nature of light-

24 absorbing carbonaceous aerosols, Atmos. Chem. Phys., 6, 3131–3148, doi:10.5194/acp-6-

25 3131–2006, 2006.

26 Bahreini, R. Ervens, B., Middlebrook, A. M., Warneke, C., de Gouw, J. A., DeCarlo, P. F.,

27 Jimenez, J. L., Atlas, E., Brioude, J., Brock, C. A., Fried, A., Holloway, J. S., Peischl, J.,

28 Richter, D., Ryerson, T. B., Stark, H., Walega, J., Weibring, P., Wollny, A. G., and

29 Fehsenfeld, F. C.: Organic Aerosol Formation in Urban and Industrial plumes near Houston

30 and Dallas, TX, J. Geophys. Res., 114, D00F16, doi:10.1029/2008JD011493, 2009.

Bey, I., Jacob, D. J., Yantosca, R. M., Logan, J. A., Field, B. D., Fiore, A. M., Li, Q., Liu, H. Y., Mickley, L. J., and Schultz, M. G.: Global modeling of tropospheric chemistry with assimilated meteorology: Model description and evaluation, J. Geophys. Res., 106, 23073–23078, 2001.

Bian, H., Prather, M. J., and Takemura, T.: Tropospheric aerosol impacts on trace gas budgets through photolysis, J. Geophys. Res., 108, 4242, doi:10.1029/2002JD002743, 2003.

Bond, T. C. and Bergstrom, R. W.: Light absorption by carbonaceous particles: an investigative review, Aerosol Sci. Tech., 40, 27–67, doi:10.1080/02786820500421521, 2006.

Bond, T. C., Doherty, S. J., Fahey, D. W., Forster, P. M., Berntsen, T., DeAngelo, B. J., Flanner, M. G., Ghan, S., Kärcher, B., Koch, D., Kinne, S., Kondo, Y., Quinn, P. K., Sarofim, M. C., Schultz, M. G., Schulz, M., Venkataraman, C., Zhang, H., Zhang, S., Bellouin, N., Guttikunda, S. K., Hopke, P. K., Jacobson, M. Z., Kaiser, J. W., Klimont, Z., Lohmann, U., Schwarz, J. P., Shindell, D., Storelvmo, T., Warren, S. G., and Zender, C. S.: Bounding the role of black carbon in the climate system: A scientific assessment, J. Geophys. Res., 118, 5380–5552, doi:10.1002/jgrd.50171, 2013.

Canagaratna, M.R., Jayne, J.T., Jimenez, J.L., Allan, J.D., Alfarra, M.R, Zhang, Q., Onasch, T.B., Drewnick, F., Coe, H., Middlebrook, A., Delia, A., Williams, L.R., Trimborn, A.M., Northway, M.J., DeCarlo, P.F., Kolb, C.E., Davidovits, P., Worsnop, D.R. Chemical and Microphysical Characterization of Ambient Aerosols with the Aerodyne Aerosol Mass Spectrometer. Mass Spectrometry Reviews, 26, 185– 222, 2007.

Cai, Y., Montague, D. C., and Deshler, T.: Comparison of measured and calculated scattering from surface aerosols with an average, a size-dependent, and a time-dependent refractive index, J. Geophys. Res., 116, D02202, doi:10.1029/2010JD014607, 2011..

Cappa, C. D., Onasch, T. B., Massoli, P., Worsnop, D. R., Bates, T. S., Cross, E. S., Davidovits, P., Hakala, J., Hayden, K. L., Jobson, B. T., Kolesar, K. R., Lack, D. A., Lerner, B. M., Li, S.-M., Mellon, D., Nuaaman, I., Olfert, J. S., Petäjä, T., Quinn, P. K., Song, C., Subramanian, R., Williams, E. J., and Zaveri, R. A.: Radiative Absorption Enhancements Due to the Mixing State of Atmospheric Black Carbon, Science, 337, 1078–1081, doi:10.1126/science.1223447, 2012.

Chin, M., Ginoux, P., Kinne, S., Holben, B. N., Duncan, B. N., Martin, R. V., Logan, J. A., Higurashi, A., and Nakajima, T.: Tropospheric aerosol optical thickness from the GOCART

model and comparisons with satellite and sun photometer measurements, J. Atmos. Sci., 59, 461–483, 2002.

Chin, M., Diehl, T., Dubovik, O., Eck, T. F., Holben, B. N., Sinyuk, A., and Streets, D. G., Light absorption by pollution, dust, and biomass burning aerosols: a global model study and evaluation with AERONET measurements, Ann. Geophys., 27, 3439–3464, doi:10.5194/angeo-27-3439-2009, 2009.

Chung, C. E., Ramanathan, V., and Decremer, D.: Observationally constrained estimates of carbonaceous aerosol radiative forcing, PNAS, 109, 11624–11629, doi:10.1073/pnas.1203707109, 2012.

Cubison, M. J., Ortega, A. M., Hayes, P. L., Farmer, D. K., Day, D., Lechner, M. J., Brune, W. H., Apel, E., Diskin, G. S., Fisher, J. A., Fuelberg, H. E., Hecobian, A., Knapp, D. J., Mikoviny, T., Riemer, D., Sachse, G. W., Sessions, W., Weber, R. J., Weinheimer, A. J., Wisthaler, A., and Jimenez, J. L.: Effects of aging on organic aerosol from open biomass burning smoke in aircraft and laboratory studies, Atmos. Chem. Phys., 11, 12049-12064, doi:10.5194/acp-11-12049-2011, 2011.

DeCarlo, P., Slowik, J.G., Worsnop, D.R., Davidovits, P., and Jimenez, J.L. Particle Morphology and Density Characterization by Combined Mobility and Aerodynamic Diameter Measurements. Part 1: Theory. Aerosol Science and Technology, 38: 1185–1205, 2004. DOI: 10.1080/027868290903907.

DeCarlo, P. F., Dunlea, E. J., Kimmel, J. R., Aiken, A. C., Sueper, D., Crounse, J., Wennberg, P. O., Emmons, L., Shinozuka, Y., Clarke, A., Zhou, J., Tomlinson, J., Collins, D. R., Knapp, D., Weinheimer, A. J., Montzka, D. D., Campos, T., and Jimenez, J. L.: Fast airborne aerosol size and chemistry measurements above Mexico City and Central Mexico during the MILAGRO campaign, Atmos. Chem. Phys., 8, 4027–4048, doi:10.5194/acp-8-4027–2008, 2008.

Dibb, J. E., Talbot, R. W., Scheuer, E., Seid, G., Avery, M. A., and Singh, H. B.: Aerosol chemical composition in Asian continental outflow during TRACE-P: Comparison to PEM-West B, J. Geophys. Res., 108 (D21), 8815, doi:10.1029/2002JD003111, 2003.

Drury, E. E., Jacob, D. J., Spurr, R. J. D., Wang, J., Shinozuka, Y., Anderson, B. E., Clarke, A. D., Dibb, J., McNaughton, C., and Weber, R. J.: Synthesis of satellite (MODIS), aircraft (ICARTT), and surface (IMPROVE, EPA-AQS, AERONET) aerosol observations over

eastern North America to improve MODIS aerosol retrievals and constrain aerosol concentrations and sources, J. Geophys. Res., 115, D14204, doi:10.1029/2009JD012629, 2010.

Dubovik, O. and King, M. D.: A flexible inversion algorithm for retrieval of aerosol optical properties from Sun and sky radiance measurements, J. Geophys. Res., 105, 20673–20696, 2000.

Duncan, B. N., Strahan, S. E., Yoshida, Y., Steenrod, S. D., and Livesey, N.: Model study of the cross-tropopause transport of biomass burning pollution, Atmos. Chem. Phys., 7, 3713–3736, doi:10.5194/acp-7-3713-2007, 2007.

Esteve, A. R., Highwood, E. J., Morgan, W. T., Allen, G., Coe, H., Grainger, R. G., Brown, P., and Szpek, K.: A study on the sensitivities of simulated aerosol optical properties to composition and size distribution using airborne measurements, Atmos. Environ., 89, 517-524, doi:10.1016/j.atmosenv.2014.02.063, 2014.

Fredenslund, A., J. Gmehling, and P. Rasmussen, Vapor-Liquid Equilibria Using UNIFAC, A Group Contribution Method, Elsevier, Amsterdam, 1977.

Forrister, H., Liu, J., Scheuer, E., Dibb, J., Ziemba, L., Thornhill, K. L., Anderson, B., Diskin, G., Perring, A. E., Schwarz, J. P., Campuzano-Jost, P., Day, D. A., Palm, B. B., Jimenez, J. L., Nenes, A., and Weber, R. J.: Evolution of brown carbon in wildfire plumes. Geophys. Res. Lett., 42, 4623–4630. doi: 10.1002/2015GL063897, 2015.

Fountoukis, C. and Nenes, A.: ISORROPIA II: A computationally efficient thermodynamic equilibrium model for K^+–Ca^{2+}–Mg^{2+}–NH_4^+–Na^+–SO_4^{2-}–NO_3^-–Cl^-–H_2O aerosols, Atmospheric Chemistry and Physics, 7, 4639–4659, 2007.

Ginoux, P., Chin, M., Tegen, I., Prospero, J., Holben, B., Dubovik, O., and Lin, S.-J.: Sources and global distributions of dust aerosols simulated with the GOCART model, J. Geophys. Res., 106, 20,255–20,273, 2001.

Ginoux, P., Prospero, J., Torres, O., and Chin, M.: Long-term simulation of dust distribution with the GOCART model: Correlation with the North Atlantic Oscillation, Environ. Modeling and Software, 19, 113–128, 2004.

He, S., and Carmichael, G.: Sensitivity of photolysis rates and O_3 production in the troposphere to aerosol properties, J. Geophys. Res., 104, 26307–26324, 1991.

1 Heald, C. L., Ridley, D. A., Kroll, J. H., Barrett, S. R. H., Cady-Pereira, K. E., Alvarado, M.
2 J., and Holmes, C. D.: Contrasting the direct radiative effect and direct radiative forcing of
3 aerosols, Atmos. Chem. Phys., 14, 5513–5527, doi:10.5194/acp-14-5513-2014, 2014.

4 Hess, M., Koepke, P., and Schult, I.: Optical Properties of Aerosols and clouds: The software
5 package OPAC, Bull. Am. Met. Soc., 79, 831–844, 1998.

6 Highwood, E. J., Northway, M. J., McMeeking, G. R., Morgan, W. T., Liu, D., Osborne, S.,
7 Bower, K., Coe, H., Ryder, C., and Williams, P.: Aerosol scattering and absorption during the
8 EUCAARI-LONGREX flights of the Facility for Airborne Atmospheric Measurements
9 (FAAM) BAe-146: can measurements and models agree?, Atmos. Chem. Phys., 12, 7251-
10 7267, doi:10.5194/acp-12-7251-2012, 2012.

11 Huffman, J. A., Jayne, J. T., Drewnick, F., Aiken, A. C., Onasch, T., Worsnop, D. R., and
12 Jimenez, J. L.: Design, Modeling, Optimization, and Experimental Tests of a Particle Beam
13 Width Probe for the Aerodyne Aerosol Mass Spectrometer, Aerosol Sci. and Technol., 39,
14 1143-1163, doi:10.1080/02786820500423782, 2005.

15 Iacono, M. J., Delamere, J. S., Mlawer, E. J., Shephard, M. W., Clough, S. A., and Collins,
16 W. D.: Radiative forcing by long-lived greenhouse gases: calculations with the AER radiative
17 transfer models, J. Geophys. Res.-Atmos., 113, D13103, doi:10.1029/2008jd009944, 2008.

18 Jacob, D. J., Crawford, J. H., Maring, H., Clarke, A. D., Dibb, J. E., Emmons, L. K., Ferrare,
19 R. A., Hostetler, C. A., Russell, P. B., Singh, H. B., Thompson, A. M., Shaw, G. E.,
20 McCauley, E., Pederson, J. R., and Fisher, J. A.: The Arctic Research of the Composition of
21 the Troposphere from Aircraft and Satellites (ARCTAS) mission: design, execution, and first
22 results, Atmos. Chem. Phys., 10, 5191–5212, doi:10.5194/acp-10-5191-2010, 2010.

23 Jacobson, M. Z.: Development and application of a new air pollution modeling system - II.
24 Aerosol module structure and design, Atmos. Environ., 31, 131–144, 1997.

25 Jacobson, M. Z.: Studying the effects of aerosols on vertical photolysis rate coefficient and
26 temperature profiles over an urban airshed, J. Geophys. Res., 103, 10593–10604, 1998.

27 Jacobson, M. Z.: Strong radiative heating due to the mixing state of black carbon in
28 atmospheric aerosols, Nature, 409, 695–697, 2001.

Jacobson, M. Z.: Analysis of aerosol interactions with numerical techniques for solving coagulation, nucleation, condensation, dissolution, and reversible chemistry among multiple size distributions, J. Geophys. Res., 107, 4366, doi:10.1029/2001JD002,044, 2002.

Jacobson, M. Z.: Fundamentals of Atmospheric Modeling, 2nd ed., Cambridge University Press, 2005.

Jaeglé, L., Quinn, P. K., Bates, T. S., Alexander, B., and Lin, J.-T.: Global distribution of sea salt aerosols: new constraints from in situ and remote sensing observations, Atmos. Chem. Phys., 11, 3137–3157, doi:10.5194/acp-11-3137-2011, 2011.

Jimenez, J. L., Canagaratna, M. R., Donahue, N. M., Prevot, A. S. H., Zhang, Q., Kroll, J. H., DeCarlo, P. F., Allan, J. D., Coe, H., Ng, N. L., Aiken, A. C., Docherty, K. S., Ulbrich, I. M., Grieshop, A. P., Robinson, A. L., Duplissy, J., Smith, J. D., Wilson, K. R., Lanz, V. A., Hueglin, C., Sun, Y. L., Tian, J., Laaksonen, A., Raatikainen, T., Rautiainen, J, Vaattovaara, P., Ehn, M., Kulmala, M., Tomlinson, J. M., Collins, D. R., Cubison, M. J., Dunlea, E. J., Huffman, J. A., Onasch, T. B., Alfarra, M. R., Williams, P. I., Bower, K., Kondo, Y., Schneider, J., Drewnick, F., Borrmann, S., Weimer, S., Demerjian, K., Salcedo, D., Cottrell, L., Griffin, R., Takami, A., Miyoshi, T, Hatakeyama, S., Shimono, A., Sun, J. Y., Zhang, Y. M., Dzepina, K., Kimmel, J. R., Sueper, D., Jayne, J. T., Herndon, S. C., Trimborn, A. M., Williams, L. R., Wood, E. C., Middlebrook, A. M., Kolb, C. E., Baltensperger, U., and Worsnop, D. R.: Evolution of Organic Aerosols in the Atmosphere, Science, 326,1525–1529, 2009.

Kassianov, E., Berg, L. K., Pekour, M., Barnard, J., Chand, D., Flynn, C., Ovchinnikov, M., Sedlacek, A., Schmid, B., Shilling, J., Tomlinson, J., and Fast, J.: Airborne aerosol in situ measurements during TCAP: A closure study of total scattering. Atmosphere, 6, 1069-1101, doi:10.3390/atmos6081069, 2015.

Kim, D., Wang, C., kman, A. M. L., Barth, M. C., and Rasch, P. J.: Distribution and direct radiative forcing of carbonaceous and sulfate aerosols in an interactive size-resolving aerosol–climate model, J. Geophys. Res., 113, D16309, doi:10.1029/2007JD009756, 2008.

Kim, Y. P., Seinfeld, J. H., and Saxena, P.: Atmospheric gas-aerosol equilibrium I. thermodynamic model, Aerosol Science and Technology, 19, 157–181, 1993.

Kleinman, L. I., Sedlacek, A. J., III, Yokelson, R. J., Onasch, T. B., Adachi, K., Buseck, P. R., Chand, D., Collier, S., Dubey, M. K., Mei, F., Shilling, J. E., Springston, S. R., Wang, J.,

Wigder, N. L., and Zhang, Q.: Time Dependence of Aerosols in Biomass Burn Plumes from BBOP, American Geophysical Union, Fall Meeting 2014, Abstract #A52A-01, 2014.

Kondo, Y., Oshima, N., Kajino, M., Mikami, R., Moteki, N., Takegawa, N., Verma, R. L., Kajii, Y., Kato, S., and Takami, A.: Emissions of black carbon in East Asia estimated from observations at a remote site in the East China Sea, J. Geophys. Res., 116, D16201, doi:10.1029/2011JD015637, 2011.

Kusik, C., and Meissner, H.: Electrolyte activity coefficients in inorganic processing, in Fundamental Aspects of Hydrometallurgical Processes, AIChE Symposium Series, edited by T. Chapman, L. Taularides, G. Hubred, and R. Wellek, pp. 14–20, AIChE, New York, 1978.

Lack, D. A., Cappa, C. D., Covert, D. S., Baynard, T., Massoli, P., Sierau, B., Bates, T. S., Quinn, P. K., Lovejoy, E. R., and Ravishankara, A. R.: Bias in Filter-Based Aerosol Light Absorption Measurements Due to Organic Aerosol Loading: Evidence from Ambient Measurements, Aerosol Science and Technology, 42, 1033–1041, doi:10.1080/02786820802389277, 2008.

Lack, D. A. and Cappa, C. D.: Impact of brown and clear carbon on light absorption enhancement, single scatter albedo and absorption wavelength dependence of black carbon, Atmos. Chem. Phys., 10, 4207–4220, doi:10.5194/acp-10-4207-2010, 2010.

Lack, D. A., J. M. Langridge, R. Bahreini, C. D. Cappa, A. M. Middlebrook, and J. P. Schwarz. Brown carbon and internal mixing in biomass burning particles, PNAS, 109, 14802-14807, doi:10.1073/pnas.1206575109, 2012.

Lefer, B. L., Shetter, R. E., Hall, S. R., Crawford, J. H., and J. R.: Impact of clouds and aerosols on photolysis frequencies and photochemistry during TRACE-P: 1. Analysis using radiative transfer and photochemical box models, J. Geophys. Res., 108, 8821, doi:10.1029/2002JD003171, 2003.

Li, G., Zhang, R., Fan, J., and Tie, X.: Impacts of black carbon aerosol on photolysis and ozone, J. Geophys. Res., 110, D23206, doi:10.1029/2005JD005898, 2005.

Liao, H., Yung, Y., and Seinfeld, J.: Effects of aerosols on tropospheric photolysis rates in clear and cloudy atmospheres, J. Geophys. Res., 104(D19), 23697–23707, 1999.

1 Liao, H., Adams, P. J., Seinfeld, J. H., Mickley, L. J. and Jacob D. J.: Interactions between

2 tropospheric chemistry and aerosols in a unified GCM simulation, J. Geophys. Res., 108(D1),

3 4001, doi:10.1029/2001JD001260, 2003.

4 Liu, X., Penner, J. E., Das, B., Bergmann, D., Rodriguez, J. M., Strahan, S., Wang, M., and

5 Feng, Y.: Uncertainties in global aerosol simulations: Assessment using three meteorological

6 data sets, J. Geophys. Res., 112, D11212, doi:10.1029/2006JD008216, 2007.

7 Loeb, N. G. and Su, W.: Direct aerosol radiative forcing uncertainty based on a radiative

8 perturbation analysis, J. Climate 23, 5288-5293, doi:10.1175/2010JCLI3543.1, 2010.

9 Martin, R. V., Jacob, D. J., Yantosca, R. M., Chin, M., and Ginoux, P.: Global and regional

10 decreases in tropospheric oxidants from photochemical effects of aerosols, J. Geophys. Res.,

11 108, 4097, doi:10.1029/2002JD002622, 2003.

12 Maxwell Garnet, J. C.: Colours in metal glasses and in metallic films, Philos. Trans. Roy.

13 Soc. A203, 385–420, 1904.

14 Michelangeli, D., Allen, M., Yung, Y., Shia, R.-L., Crisp, D., and Eluszkiewicz, J.:

15 Enhancement of Atmospheric Radiation by an Aerosol Layer, J. Geophys. Res., 97(D1), 865–

16 874, 1992.

17 Moteki, N. and Kondo, Y.: Effects of mixing state on black carbon measurements by Laser-

18 Induced Incandescence, Aerosol Sci. Technol., 41, 398–417, 2007.

19 Moteki, N. and Kondo, Y.: Method to measure time-dependent scattering cross sections of

20 particles evaporating in a laser beam, J. Aerosol Sci., 39, 348–364, 2008.

21 Myrdal, P. B. and Yalkowsky, S. H.: Estimating pure component vapor pressures of complex

22 organic molecules, Industrial and Engineering Chemistry Research, 36, 2494–2499, 1997.

23 Nenes, A., Pandis, S. N., and Pilinis, C.: ISORROPIA: A new thermodynamic equilibrium

24 model for multiphase multicomponent inorganic aerosols, Aquatic Geochemistry, 4, 123–152,

25 1998.

26 Park, R. J., Jacob, D. J., Chin, M., and Martin, R. V.: Sources of carbonaceous aerosols over

27 the United States and implications for natural visibility, J. Geophys. Res., 108, 4355,

28 doi:10.1029/2002JD003190, 2003.

1   Petters, M. D., and Kreidenweis, S. M.: A single parameter representation of hygroscopic

2   growth and cloud condensation nucleus activity, Atmos. Chem. Phys., 7, 1961–1971,

3   doi:10.5194/acp-7-1961-2007, 2007.

4   Pun, B. K., Griffin, R. J., Seigneur, C., and Seinfeld, J. H.: Secondary organic aerosol, 2,

5   thermodynamic model for gas/particle partitioning of molecular constituents, J. Geophys.

6   Res., 107, 4333, doi:10.1029/2001JD000,542, 2002.

7   Quinn, P. K., and Coffman, D. J.: Local closure during the First Aerosol Characterization

8   Experiment (ACE 1): Aerosol mass concentration and scattering and backscattering

9   coefficients, J. Geophys. Res., 103, 16575–16596, doi:10.1029/97JD03757, 1998.

10   Reid, J. S., Brooks, B., Crahan, K. K., Hegg, D. A., Eck, T. F., O'Neill, N., de Leeuw, G.,

11   Reid, E. A., and Anderson, K. D.: Reconciliation of coarse mode sea-salt aerosol particle size

12   measurements and parameterizations at a subtropical ocean receptor site, J. Geophys. Res.,

13   111, D02202, doi:10.1029/2005JD006200, 2006.

14   Schwarz, J. P., Spackman, J. R., Fahey, D. W., Gao, R. S., Lohmann, U., Stier, P., Watts, L.

15   A., Thomson, D. S., Lack, D. A., Pfister, L., Mahoney, M. J., Baumgardner, D., Wilson, J. C.,

16   and Reeves, J. M.: Coatings and their enhancement of black carbon light absorption in the

17   tropical atmosphere, J. Geophys. Res., 113, D03203, doi:10.1029/2007JD009042, 2008.

18   Sciare, J., Oikonomou, K., Cachier, H., Mihalopoulos, N., Andreae, M. O., Maenhaut, W.,

19   and Sarda-Estève, R.: Aerosol mass closure and reconstruction of the light scattering

20   coefficient over the Eastern Mediterranean Sea during the MINOS campaign, Atmos. Chem.

21   Phys., 5, 2253-2265, doi:10.5194/acp-5-2253-2005, 2005.

22   Shiraiwa, M., Kondo, Y., Iwamoto, T., and Kita, K.: Amplification of Light Absorption of

23   Black Carbon by Organic Coating, Aerosol Sci. Tech., 44, 46–54, 2010.

24   Steele, H. D., Investigations of cloud altering effects of atmospheric aerosols using a new

25   mixed eulerian-lagrangian aerosol model, Ph.D. thesis, Massachusetts Institute of

26   Technology, 2004.

27   Stier, P., Seinfeld, J. H., Kinne, S., Feichter, J., and Boucher, O.: Impact of nonabsorbing

28   anthropogenic aerosols on clearsky atmospheric absorption, J. Geophys. Res., 111, D18201,

29   doi:10.1029/2006JD007147, 2006.

Strahan, S. E., Duncan, B. N., and Hoor, P.: Observationally derived transport diagnostics for the lowermost stratosphere and their application to the GMI chemistry and transport model, Atmos. Chem. Phys., 7, 2435–2445, doi:10.5194/acp-7-2435-2007, 2007.

Sullivan, A., Peltier, R. E., Brock, C. A., de Gouw, J. A., Holloway, J. S., Warneke, C., Wollny, A. G., and Weber, R. J.: Airborne measurements of carbonaceous aerosol soluble in water over northeastern United States: Method development and an investigation into water-soluble organic carbon sources, J. Geophys. Res., 111, D23S46, doi:10.1029/2006JD007072, 2006.

Tang, I. N.: Thermodynamic and optical properties of mixed-salt aerosols of atmospheric importance, J. Geophys. Res., 102, 1883–1893, 1997.

Tang, I. N., Tridico, A., and Fung, K.: Thermodynamic and optical properties of sea salt aerosols, J. Geophys. Res., 102, 23,269–23,275, 1997.

Tang, Y., Carmichael, G. R., Uno, I., Woo, J-H., Kurata, G., Lefer, B., Shetter, R. E., Huang, H., Anderson, B. E., Avery, M. A., Clarke, A. D. and Blake, D. R.: Impacts of aerosols and clouds on photolysis frequencies and photochemistry during TRACE-P: 2. Three-dimensional study using a regional chemical transport model, J. Geophys. Res., 108(D21), 8822, doi:10.1029/2002JD003100, 2003.

Tian, J., Riemer, N., West, M., Pfaffenberger, L., Schlager, H., and Petzold, A.: Modeling the evolution of aerosol particles in a ship plume using PartMC-MOSAIC, Atmos. Chem. Phys., 14, 5327–5347, 2014.

Tie, X., Madronich, S., Walters, S., Edwards, D. P., Ginoux, P., Mahowald, N., Zhang, R., Lou, C., and Brasseur, G.: Assessment of the global impact of aerosols on tropospheric oxidants, J. Geophys. Res., 110, D03204, doi:10.1029/2004JD005359, 2005.

Toon, O. B.: An Overview of the 'Studies of Emissions and Atmospheric Composition, Clouds and Climate Coupling by Regional Surveys' (SEAC4RS) Field Mission (Invited) American Geophysical Union, Fall Meeting 2013, Abstract #A12D-01, 2013.

Toon, O., and Ackerman, T.: Algorithms for the calculation of scattering by stratified spheres, Applied Optics, 20, 3657–3660, 1981.

1   Virkkula, A.: Correction of the Calibration of the 3-wavelength Particle Soot Absorption

2   Photometer (3λ PSAP), Aerosol Science and Technology, 44, 706–712,

3   doi:10.1080/02786826.2010.482110, 2010.

4   Wang, J., Christopher, S. A., Brechtel, F., Kim, J., Schmid, B., Redemann, J., Russell, P. B.,

5   Quinn, P., and Holben, B. N.: Geostationary satellite retrievals of aerosol optical thickness

6   during ACE-Asia, J. Geophys. Res., 108, 8657, doi:10.1029/2003JD003580, D23, 2003a.

7   Wang, J., Christopher, S. A., Reid, J. S., Maring, H., Savoie, D., Holben, B. N., Livingston, J.

8   M., Russell, P. B., and Yang, S.-K.: GOES 8 retrieval of dust aerosol optical thickness over

9   the Atlantic Ocean during PRIDE, J. Geophys. Res., 108, 8595, doi:10.1029/2002JD002494,

10   D19, 2003b.

11   Wang, X., Heald, C. L., Ridley, D. A., Schwarz, J. P., Spackman, J. R., Perring, A. E., Coe,

12   H., Liu, D., and Clarke, A. D.: Exploiting simultaneous observational constraints on mass and

13   absorption to estimate the global direct radiative forcing of black carbon and brown carbon,

14   Atmos. Chem. Phys., 14, 10989–11010, doi:10.5194/acp-14-10989-2014, 2014.

15   Wex, H., Neusüß, C., Wendisch, M., Stratmann, F., Koziar, C., Keil, A., Wiedensohler, A.,

16   and Ebert, M.: Particle scattering, backscattering, and absorption coefficients: An in situ

17   closure and sensitivity study, J. Geophys. Res., 107, 8122, doi:10.1029/2000JD000234, 2002.

18   Yang, H. and Levy, H.: Sensitivity of photodissociation rate coefficients and O_3

19   photochemical tendencies to aerosols and clouds, J. Geophys. Res., 109, D24301,

20   doi:10.1029/2004JD005032, 2004.

21

1 Table 1. Lognormal mode parameters (r_g in μm, σ unitless), density (ρ, g cm^{-3}) and refractive

2 indices (n, unitless) at 550 nm and 0% RH of selected aerosol types from OPAC v3.1, GMI,

3 GEOS-Chem v9-02, and GC-RT.

Model	Parameter	BC/Soot	OC/WASO	Sea Salt (Acc. Mode)	Trop. Sulfate
OPAC v3.1	r_g	0.0118	0.0212	0.2090	0.0695
	σ	2.00	2.24	2.03	2.03
	ρ	1.0	1.8	2.2	1.7
	n	1.75-0.44i	1.53-0.006i	1.50-10^{-8}i	1.43-10^{-8}i
GMI	r_g	0.0118	0.0212	0.2090	0.05
	σ	2.0	2.0	2.0	2.0
	ρ	1.5	1.5	2.2	1.769
	n	1.75-0.44i	1.53-0.006i	1.50-10^{-8}i	1.43-10^{-8}i
GEOS-Chem v9-02	r_g	0.02	0.063	0.09	0.07
	σ	1.6	1.6	1.5	1.6
	ρ	1.0	1.8	2.2	1.7
	n	1.75-0.44i	1.53-0.006i	1.50-10^{-8}i	1.53-0.01i
GC-RT[a]	r_g	0.02	0.063	0.09	0.07
	σ	1.6	1.6	1.5	1.6
	ρ	1.8	1.8	2.2	1.7
	n	1.95-0.79i	1.53-0.006i	1.50-10^{-8}i	1.53-0.01i

4 [a]Baseline GC-RT configuration as described in Wang et al. (2014).

5

1 Table 2. Summary of results for modeling the submicron scattering coefficient throughout the

2 entire ARCTAS campaign with OPAC v3.1, GMI, GEOS-Chem v9-02, and GC-RT. The

3 mean (μ) and standard deviation (σ) of the $\log_{10}$ error distributions are shown. The correlation

4 coefficient (r^2) and slope of the linear fit between the modeled and measured values are

5 shown as well.

Wavelength	Metric	OPAC v3.1	GMI	GEOS-Chem v9-02	GC-RT[a]
	$\mu \pm \sigma$	0.07 ± 0.24	0.06 ± 0.24	0.15 ± 0.25	0.15 ± 0.24
450 nm	r^2	0.74	0.74	0.72	0.73
	Slope	0.89 ± 0.02	0.91 ± 0.02	1.01 ± 0.02	1.05 ± 0.02
	$\mu \pm \sigma$	0.15 ± 0.24	0.09 ± 0.24	0.17 ± 0.25	0.16 ± 0.24
550 nm	r^2	0.72	0.72	0.72	0.73
	Slope	0.95 ± 0.02	0.94 ± 0.02	1.05 ± 0.02	1.08 ± 0.03
	$\mu \pm \sigma$	0.27 ± 0.25	-0.05 ± 0.27	-0.04 ± 0.24	-0.09 ± 0.25
700 nm	r^2	0.70	0.58	0.72	0.71
	Slope	1.19 ± 0.03	0.63 ± 0.01	0.68 ± 0.02	0.63 ± 0.02

6 [a]Baseline GC-RT configuration as described in Wang et al. (2014).

7

1 Table 3. Summary of results for modeling the submicron absorption coefficient (using the

2 correction of Lack et al., 2008) throughout the entire ARCTAS campaign with OPAC v3.1,

3 GMI, GEOS-Chem v9-02, and GC-RT. The mean (μ) and standard deviation (σ) of the $\log_{10}$

4 error distributions are shown. The correlation coefficient (r^2) and slope of the linear fit

5 between the modeled and measured values are shown as well.

Wavelength	Metric	OPAC v3.1	GMI	GEOS-Chem v9-02	GC-RT[a]
	$\mu \pm \sigma$	0.12 ± 0.28	0.04 ± 0.27	0.26 ± 0.26	0.20 ± 0.26
470 nm	r^2	0.70	0.72	0.69	0.70
	Slope	0.81 ± 0.06	0.83 ± 0.04	1.09 ± 0.05	0.96 ± 0.04
	$\mu \pm \sigma$	0.28 ± 0.29	0.06 ± 0.27	0.27 ± 0.25	0.22 ± 0.25
532 nm	r^2	0.70	0.71	0.68	0.69
	Slope	0.94 ± 0.06	0.94 ± 0.05	1.21 ± 0.06	1.07 ± 0.06
	$\mu \pm \sigma$	0.14 ± 0.29	0.00 ± 0.24	0.15 ± 0.25	0.09 ± 0.24
660 nm	r^2	0.68	0.68	0.65	0.67
	Slope	0.99 ± 0.10	0.75 ± 0.04	0.95 ± 0.06	0.84 ± 0.05

6 [a]Baseline GC-RT configuration as described in Wang et al. (2014).

7

1

2 Table 4. Summary of results for modeling the submicron single scattering albedo (SSA, using

3 the correction of Lack et al., 2008) throughout the entire ARCTAS campaign with OPAC

4 v3.1, GMI, GEOS-Chem v9-02, and GC-RT. The mean (μ) and standard deviation (σ) of the

5 absolute error distributions are shown. The correlation coefficient (r^2) and slope of the linear

6 fit between the modeled and measured values are shown as well.

Wavelength	Metric	OPAC v3.1	GMI	GEOS-Chem v9-02	GC-RT[a]
450 nm	$\mu \pm \sigma$	-0.01 ± 0.05	0.01 ± 0.05	-0.01 ± 0.05	0.00 ± 0.05
	r^2	0.17	0.07	0.09	0.10
	Slope	0.44 ± 0.03	0.65 ± 0.05	0.70 ± 0.04	0.61 ± 0.04
550 nm	$\mu \pm \sigma$	-0.01 ± 0.05	0.01 ± 0.05	-0.01 ± 0.05	-0.01 ± 0.05
	r^2	0.15	0.06	0.10	0.10
	Slope	0.43 ± 0.04	0.69 ± 0.06	0.73 ± 0.04	0.66 ± 0.04
700 nm	$\mu \pm \sigma$	0.01 ± 0.06	0.02 ± 0.07	-0.02 ± 0.06	-0.02 ± 0.06
	r^2	0.14	0.03	0.11	0.10
	Slope	0.32 ± 0.02	0.78 ± 0.14	0.79 ± 0.04	0.81 ± 0.04

7 [a]Baseline GC-RT configuration as described in Wang et al. (2014).

8

1 Table 5.Summary of results for modeling the submicron scattering coefficient throughout the

2 entire ARCTAS campaign for ASP v2.1 using different mixing rules. The mean (μ) and

3 standard deviation (σ) of the $\log_{10}$ error distributions are shown. The correlation coefficient

4 (r^2) and slope of the linear fit between the modeled and measured values are shown as well.

Wavelength	Metric	ASP v2.1 CS	ASP v2.1 EXT	ASP v2.1 VA	ASP v2.1 MG
	$\mu \pm \sigma$	-0.03 ± 0.17	-0.02 ± 0.17	-0.03 ± 0.17	-0.03 ± 0.17
450 nm	r^2	0.89	0.89	0.89	0.89
	Slope	0.99 ± 0.02	1.01 ± 0.02	0.99 ± 0.02	1.00 ± 0.02
	$\mu \pm \sigma$	-0.03 ± 0.17	-0.02 ± 0.17	-0.03 ± 0.17	-0.03 ± 0.17
550 nm	r^2	0.89	0.89	0.89	0.89
	Slope	1.00 ± 0.02	1.02 ± 0.02	1.00 ± 0.02	1.01 ± 0.02
	$\mu \pm \sigma$	-0.01 ± 0.17	0.00 ± 0.17	-0.01 ± 0.17	0.00 ± 0.17
700 nm	r^2	0.88	0.88	0.88	0.88
	Slope	1.07 ± 0.03	1.10 ± 0.03	1.08 ± 0.03	1.08 ± 0.03

5
6
7

1   Table 6. Summary of results for modeling the submicron absorption coefficient (using the

2   correction of Lack et al., 2008) throughout the entire ARCTAS campaign for ASP v2.1 using

3   different mixing rules. The mean (μ) and standard deviation (σ) of the $\log_{10}$ error distributions

4   are shown. The correlation coefficient (r^2) and slope of the linear fit between the modeled and

5   measured values are shown as well.

| Wavelength	Metric	ASP v2.1 CS	ASP v2.1 EXT	ASP v2.1 VA	ASP v2.1 MG	ASP v2.1 Variable
470 nm	$\mu \pm \sigma$	0.11 ± 0.32	-0.10 ± 0.32	0.16 ± 0.30	0.07 ± 0.32	0.04 ± 0.28
	r^2	0.47	0.50	0.47	0.47	0.45
	Slope	0.85 ± 0.09	0.54 ± 0.06	0.90 ± 0.09	0.79 ± 0.08	0.60 ± 0.08
532 nm	$\mu \pm \sigma$	0.13 ± 0.32	-0.05 ± 0.31	0.17 ± 0.30	0.09 ± 0.32	0.07 ± 0.28
	r^2	0.46	0.48	0.47	0.47	0.44
	Slope	0.93 ± 0.12	0.62 ± 0.09	0.98 ± 0.13	0.85 ± 0.11	0.68 ± 0.11
660 nm	$\mu \pm \sigma$	0.13 ± 0.32	0.00 ± 0.32	0.17 ± 0.30	0.09 ± 0.32	0.09 ± 0.29
	r^2	0.46	0.47	0.46	0.46	0.44
	Slope	0.97 ± 0.16	0.72 ± 0.13	1.02 ± 0.16	0.89 ± 0.14	0.76 ± 0.14

6
7

1 Table 7. Summary of results for modeling the SSA (using the correction of Lack et al., 2008)

2 throughout the entire ARCTAS campaign for ASP v2.1 using different mixing rules. The

3 mean (μ) and standard deviation (σ) of the absolute error distributions are shown. The

4 correlation coefficient (r^2) and slope of the linear fit between the modeled and measured

5 values are shown as well.

Wavelength	Metric	ASP v2.1 CS	ASP v2.1 EXT	ASP v2.1 VA	ASP v2.1 MG	ASP v2.1 Variable
	$\mu \pm \sigma$	-0.02 ± 0.04	0.01 ± 0.03	-0.03 ± 0.04	-0.01 ± 0.04	-0.01 ± 0.04
450 nm	r^2	0.20	0.18	0.24	0.20	0.30
	Slope	0.51 ± 0.06	0.30 ± 0.03	0.64 ± 0.07	0.46 ± 0.05	0.61 ± 0.06
	$\mu \pm \sigma$	-0.04 ± 0.04	-0.01 ± 0.03	-0.04 ± 0.04	-0.03 ± 0.04	-0.03 ± 0.04
550 nm	r^2	0.20	0.17	0.25	0.20	0.30
	Slope	0.54 ± 0.06	0.32 ± 0.03	0.67 ± 0.06	0.48 ± 0.05	0.64 ± 0.06
	$\mu \pm \sigma$	-0.02 ± 0.05	0.00 ± 0.05	-0.03 ± 0.05	-0.01 ± 0.05	-0.01 ± 0.05
700 nm	r^2	0.17	0.13	0.22	0.16	0.25
	Slope	0.44 ± 0.05	0.28 ± 0.03	0.55 ± 0.05	0.38 ± 0.04	0.52 ± 0.05

6
7

44

1
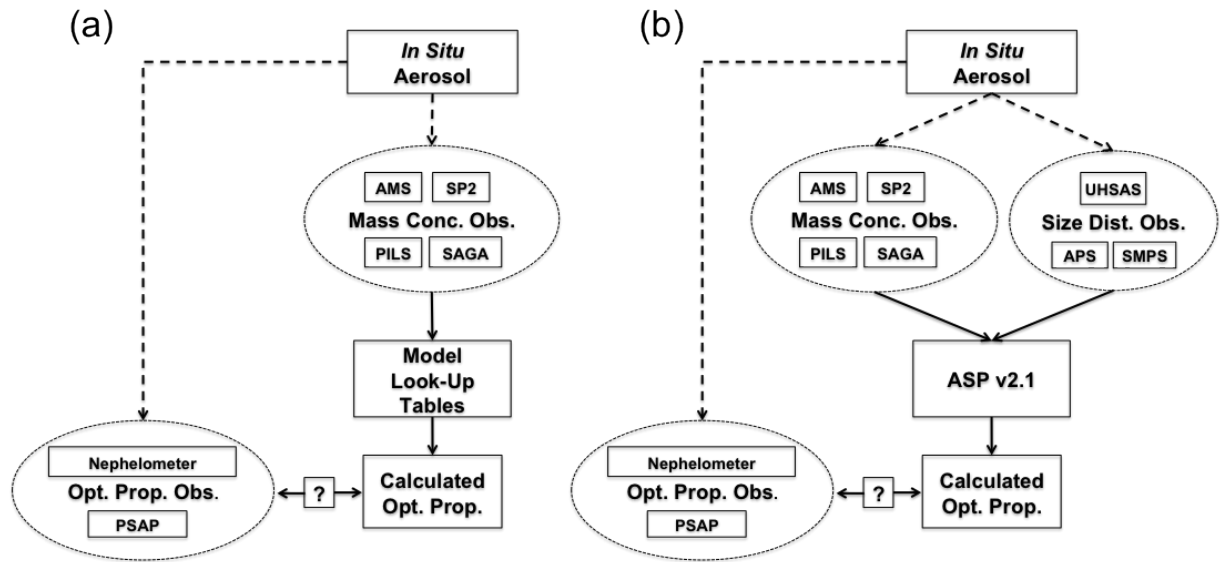
2

3

4   Figure 1. (a) Schematic of aerosol optical property closure study methodology for the OPAC

5   v3.1, NASA GMI Combo model, GEOS-Chem v9-02, and baseline GC-RT aerosol

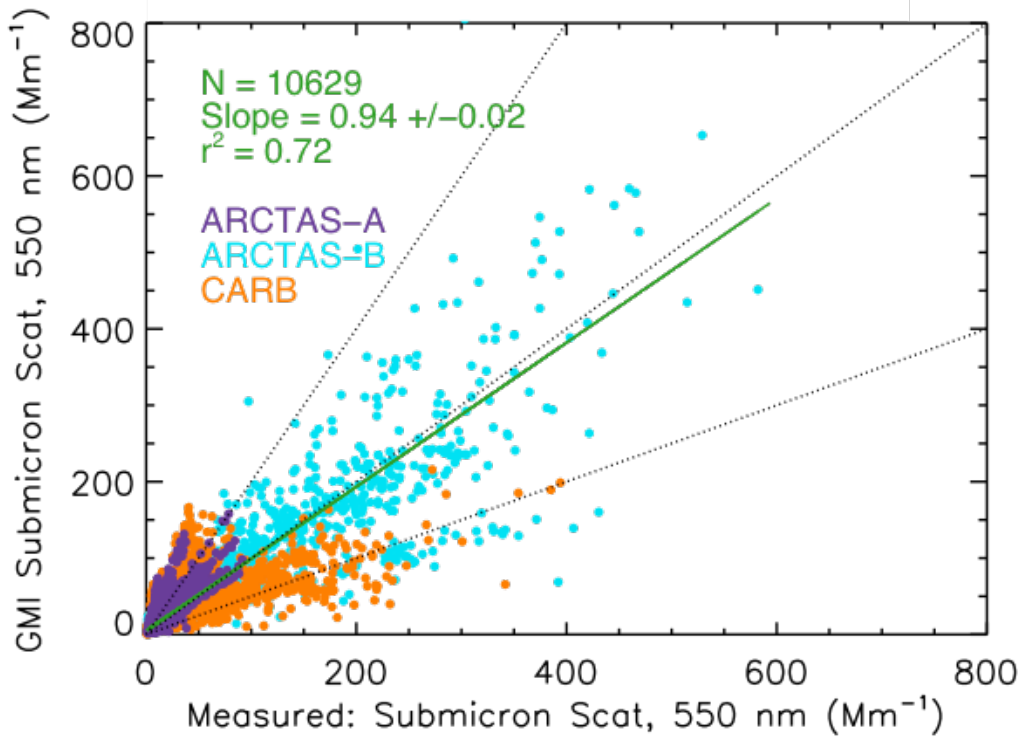6   parameterizations. (b) Schematic of closure study for ASP v2.1.

1

2

3   Figure 2. Example scatterplot of the measured submicron scattering coefficient (Mm^{-1}) at 550

4   nm versus the calculated submicron scattering coefficient for the GMI model. The color of the

5   data points corresponds to the phase of the ARCTAS campaign (ARCTAS-A in purple,

6   ARCTAS-B in cyan, and ARCTAS–CARB in orange). The dotted black lines are the 1:1 line,

7   2:1 line, and 1:2 line. The green line is the linear fit to the data. The number of data points

8   (N), the slope of the linear fit, and the correlation coefficient (r^2) are shown as well.

9

$$N = 10629$$
$$\mu = 0.09$$
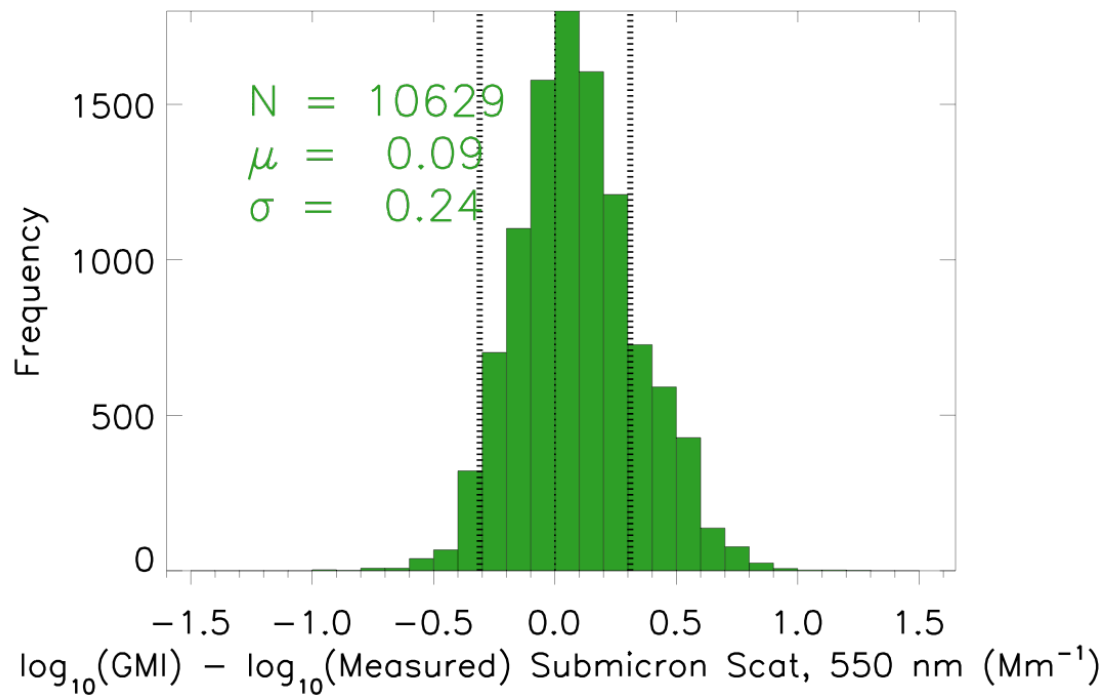$$\sigma = 0.24$$

1

2

3

4   Figure 3. Example histogram of the errors in the $\log_{10}$ of the submicron scattering coefficient

5   (modeled value – measured value) at 550 nm for the GMI model. The vertical dashed lines

6   are at ± 0.31, corresponding to an error of a factor of 2. The number of data points (*N*) and the

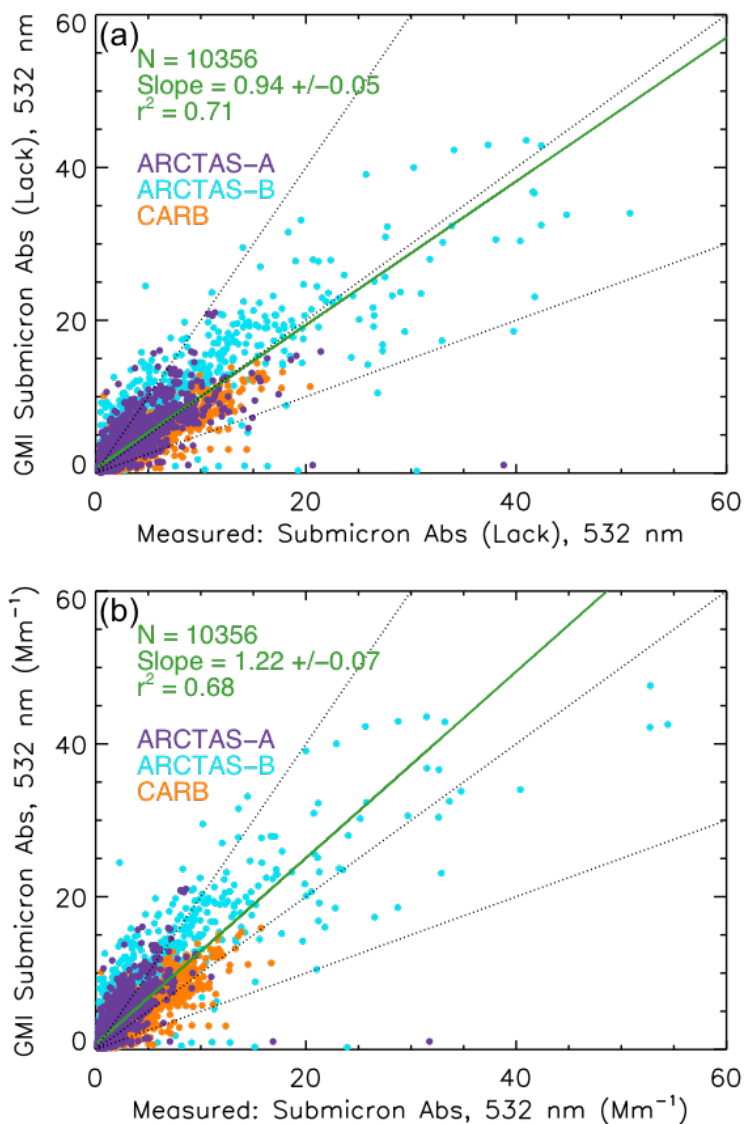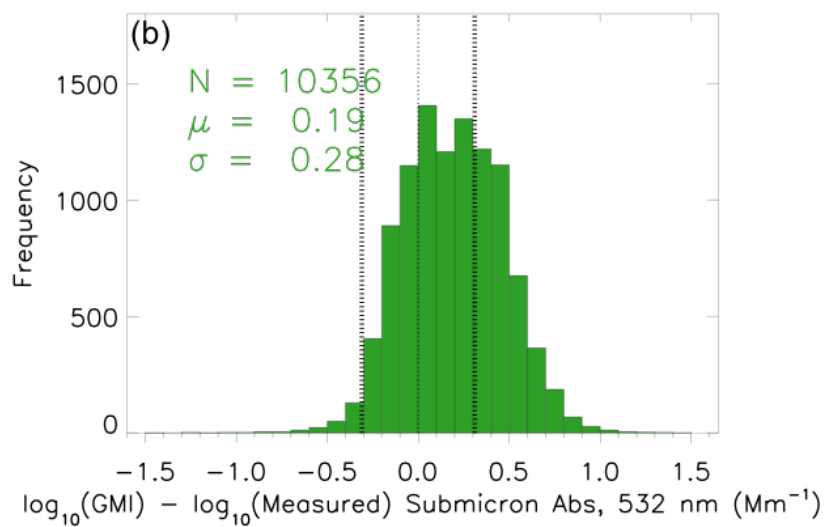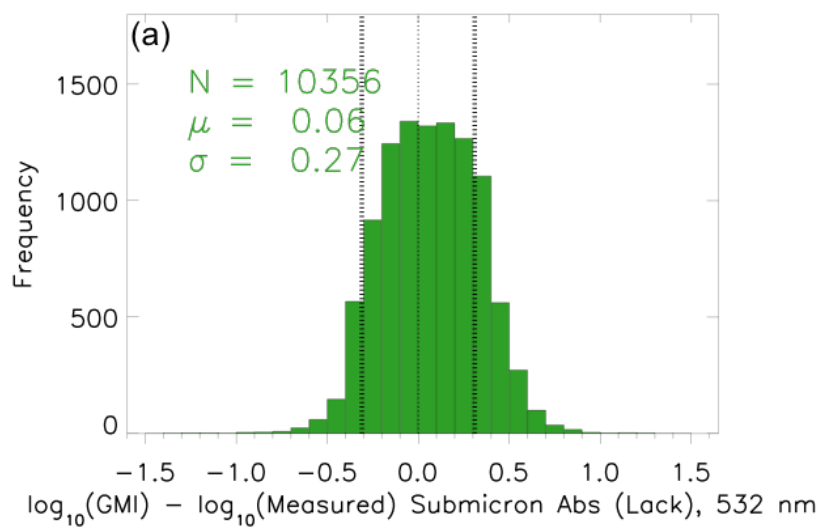7   mean (μ) and standard deviation (σ) of the error distribution are also shown.

8

Figure 4. As in Figure 2, but for submicron aerosol absorption coefficients (Mm^{-1}) at 532 nm. The PSAP measured aerosol absorption has been corrected following (a) Lack et al. (2008) and (b) Virkkula (2010).

(a)

N = 10356
μ = 0.06
σ = 0.27

log$_{10}$(GMI) − log$_{10}$(Measured) Submicron Abs (Lack), 532 nm

(b)

N = 10356
μ = 0.19
σ = 0.28

log$_{10}$(GMI) − log$_{10}$(Measured) Submicron Abs, 532 nm (Mm^{-1})

1

2

3   Figure 5. As in Figure 3, but for submicron aerosol absorption coefficients (Mm^{-1}) at 532 nm.

4   The PSAP measured aerosol absorption has been corrected following (a) Lack et al. (2008)

5   and (b) Virkkula (2010).

6

(a)

GMI SSA (Lack), 550 nm

N = 10629
Slope = 0.69 +/−0.06
r² = 0.06

ARCTAS-A
ARCTAS-B
CARB

Measured: SSA (Lack), 550 nm

(b)

N = 10629
μ = 0.01
σ = 0.05

Frequency

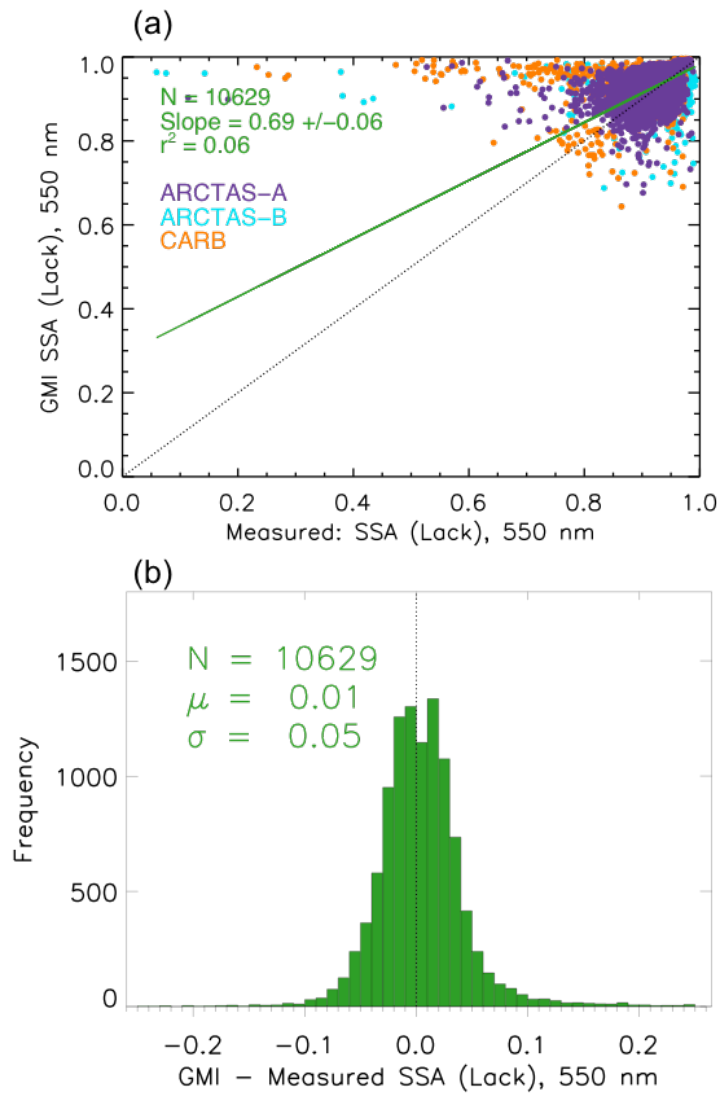GMI − Measured SSA (Lack), 550 nm

1

2

3   Figure 6. (a) Scatterplot of the measured submicron single scattering albedo (SSA) at 550 nm

4   versus the calculated submicron SSA for the GMI model. The dotted black line is the 1:1 line.

5   The green line is the linear fit to the data. (b) Histogram of the errors in the SSA (modeled
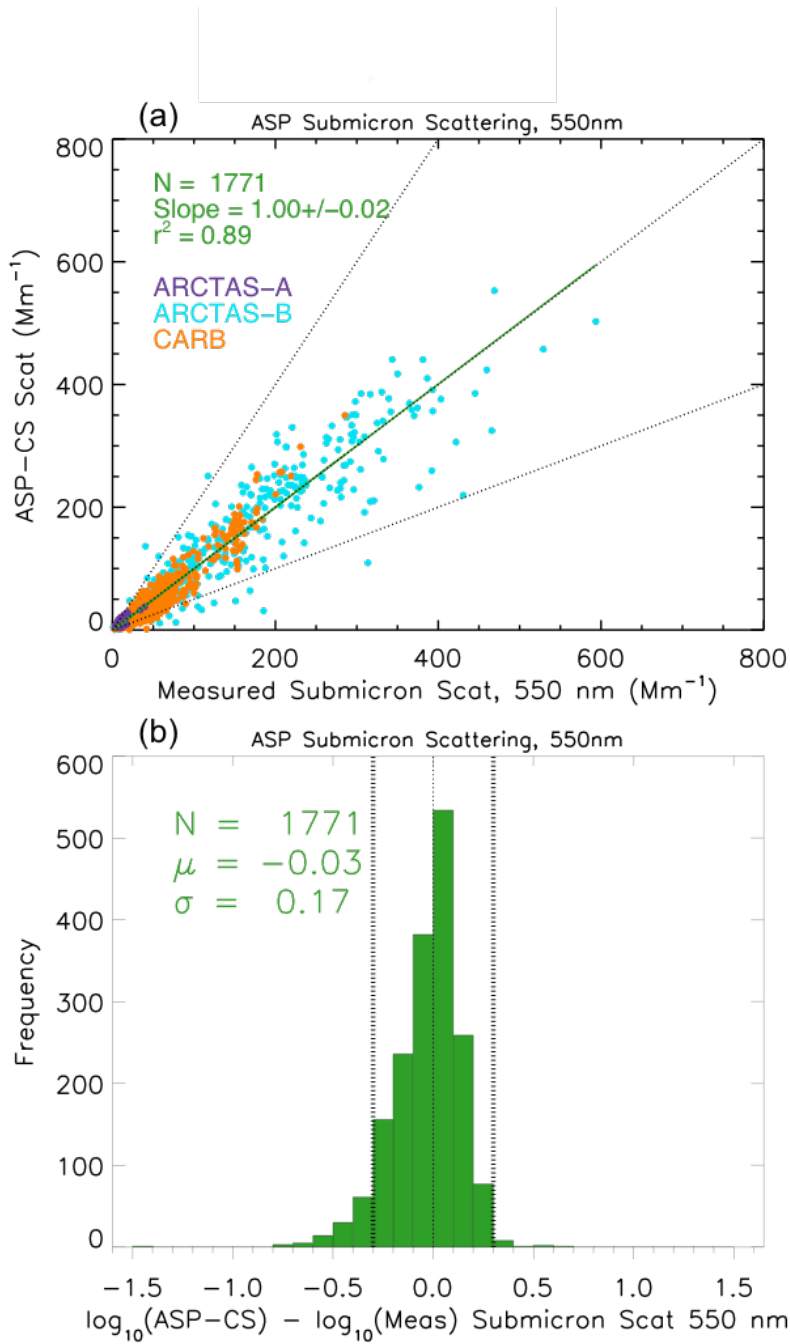
6   value – measured value) at 550 nm for the GMI model.

7

1

2

Figure 7. (a) Scatterplot of the measured submicron scattering coefficient (Mm^{-1}) at 550 nm

versus the calculated submicron scattering coefficient for ASP v2.1. The dotted black lines

are the 1:1, 2:1, and 1:2 lines. The green line is the linear fit to the data. Results for core-shell

(CS) mixing rule are shown, but the results for other mixing rules are similar (see Table 5).

(b) Histogram of the errors in the $\log_{10}$ of the submicron scattering coefficient (modeled value

– measured value) at 550 nm for ASP v2.1. The vertical dashed lines are at $\pm$ 0.31,

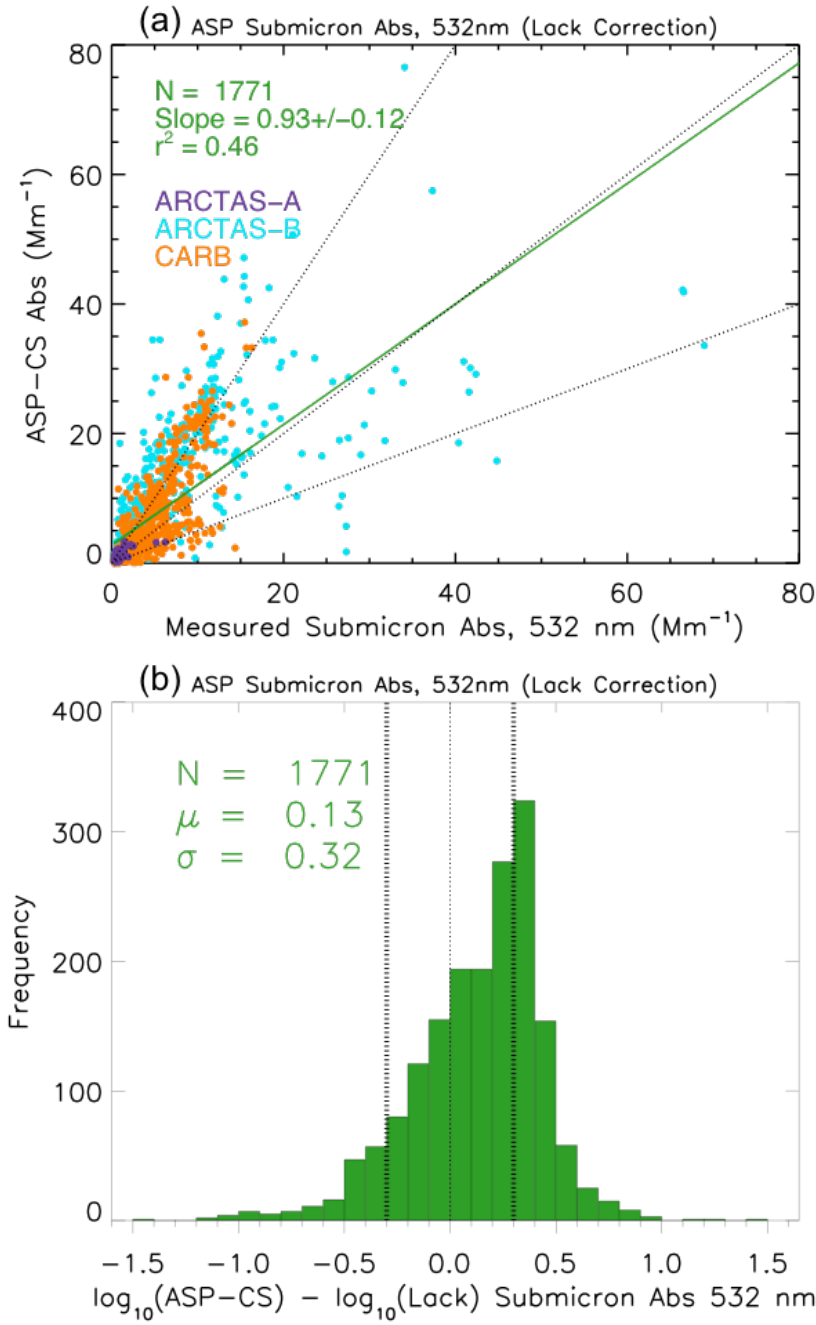corresponding to an error of a factor of 2.

Figure 8. (a) Scatterplot of the measured submicron absorption coefficient (Mm^{-1}) at 532 nm versus the calculated submicron absorption coefficient for ASP v2.1. These results use the core-shell (CS) mixing rule. (b) Histogram of the errors in the $\log_{10}$ of the submicron absorption coefficient (modeled value – measured value) at 550 nm for ASP v2.1 with the CS mixing rule.
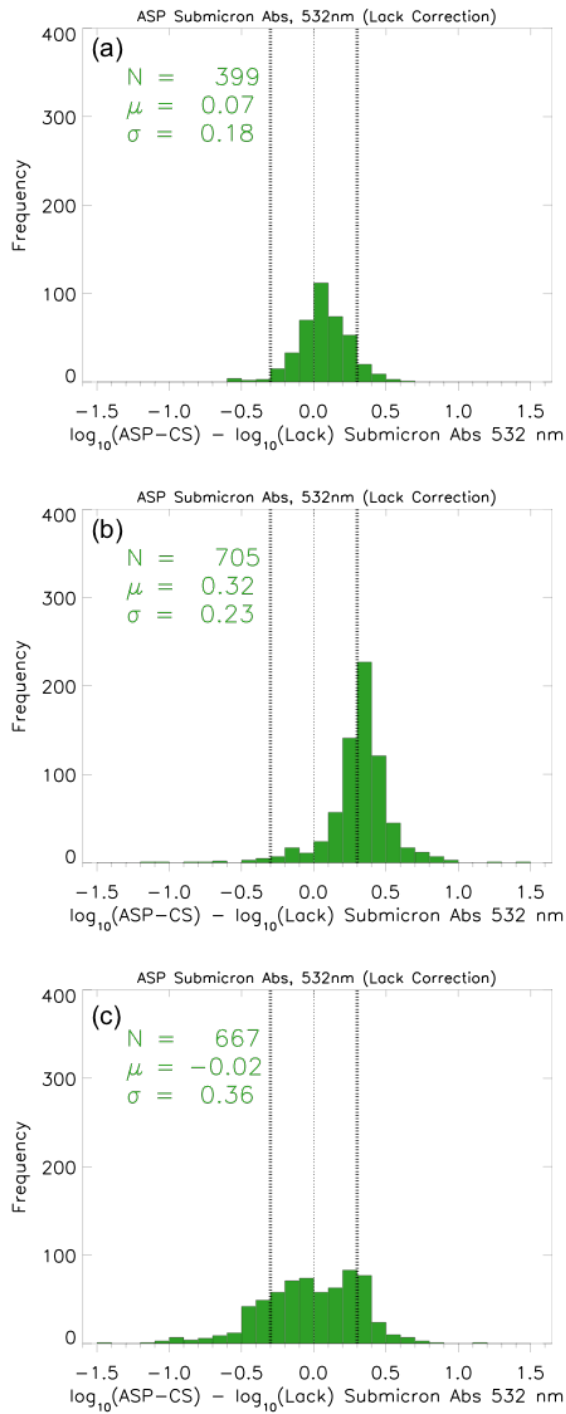
1

2

3 Figure 9. Histogram of the errors in the $\log_{10}$ of the submicron absorption coefficient

4 (modeled value – measured value) at 550 nm for ASP v2.1 with the CS mixing rule. The

5 PSAP measured aerosol absorption has been corrected following Lack et al. (2008). Results

6 are broken apart for (a) ARCTAS-A, (b) ARCTAS-B, and (c) ARCTAS-CARB.

(a) ASP Submicron Abs, 532nm (Lack Correction)

N = 1771
Slope = 0.68+/−0.11
r^2 = 0.44

ARCTAS−A
ARCTAS−B
CARB

ASP Abs − combo (Mm^{-1})

Measured Submicron Abs, 532 nm (Mm^{-1})

(b) ASP Submicron Abs, 532nm (Lack Correction)

N = 1771
μ = 0.07
σ = 0.28

Frequency

$\log_{10}$(ASP−combo) − $\log_{10}$(Lack) Submicron Abs at 532 nm
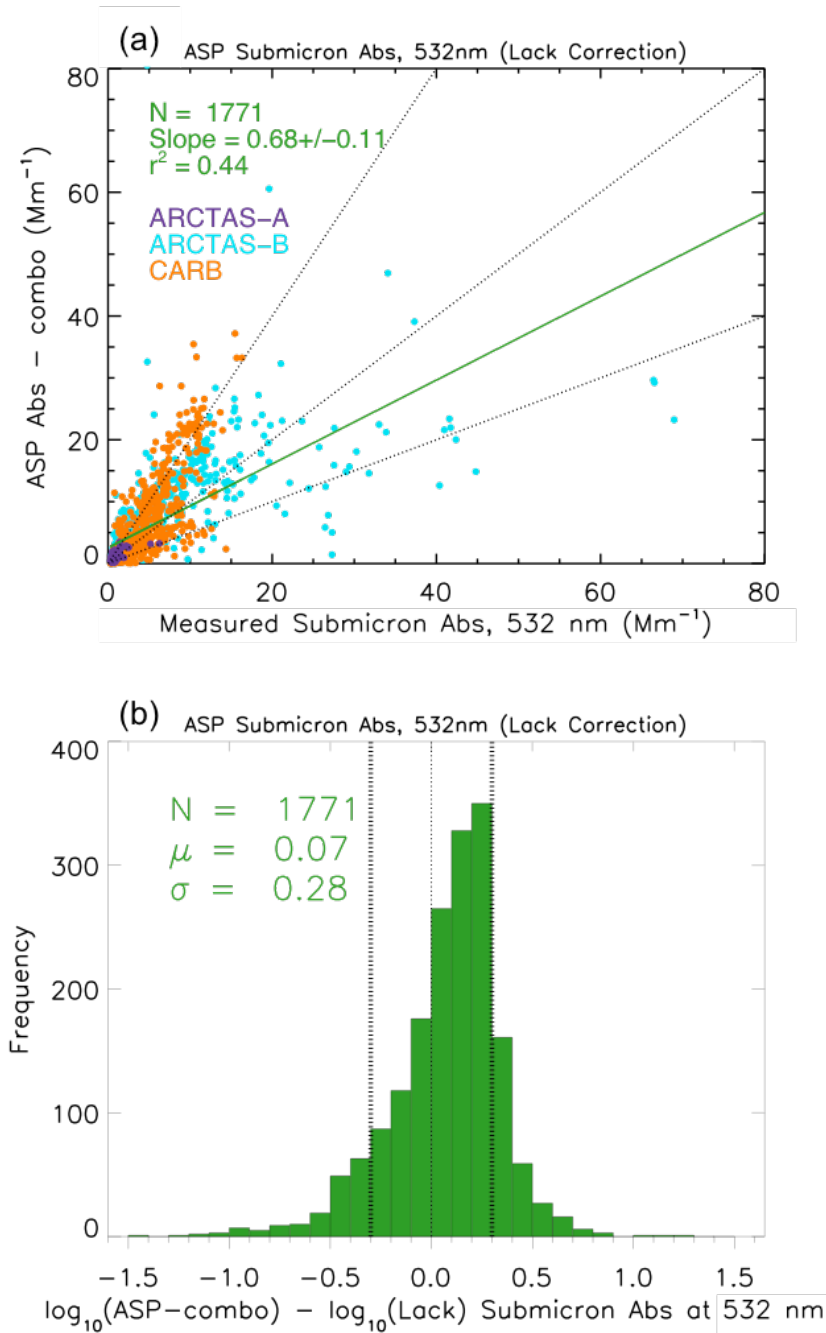
Figure 10. (a) As in Figure 8a, but using a variable mixing rule - core-shell (CS) is used for ARCTAS-A and ARCTAS-CARB, while an external mixture (EXT) is used for ARCTAS-B. (b) As in Figure 8b but with this variable mixing rule.